The cGAS-STING pathway regulates microglial chemotaxis in genome instability

Emily J. Talbot[1], Lisha Joshi[1], Peter Thornton[2], Mahya Dezfouli[3#], Kalliopi Tsafou[4],

Michael Perkinton[2] and Svetlana V. Khoronenkova[1]*

[1]Department of Biochemistry, University of Cambridge, Cambridge, UK

[2]Neuroscience, R&D BioPharmaceuticals, AstraZeneca, Cambridge, UK

[3]Translational Genomics, Discovery Biology, Discovery Sciences, BioPharmaceuticals R&D, AstraZeneca, Mölndal, Gothenburg, Sweden

[4]Department of Data Sciences & Quantitative Biology, AstraZeneca, Cambridge, UK

[#]Current address: Oligo Profiling, Mechanistic and Structural Biology, Discovery Sciences, BioPharmaceuticals R&D, AstraZeneca, Mölndal, Gothenburg, Sweden

*Corresponding author: sk870@cam.ac.uk

1 **ABSTRACT**

2 Defective DNA damage signalling and repair is a hallmark of age-related and genetic

3 neurodegenerative disease. One mechanism implicated in disease progression is DNA

4 damage-driven neuroinflammation, which is largely mediated by tissue-resident immune cells,

5 microglia. Here, we utilise human microglia-like cell models of persistent DNA damage and

6 ATM kinase deficiency to investigate how genome instability shapes microglial function. We

7 demonstrate that upon DNA damage the cytosolic DNA sensing cGAS-STING axis drives

8 chronic inflammation and a robust chemokine response, exemplified by production of CCL5

9 and CXCL10. Transcriptomic analyses revealed that cell migratory pathways were highly

10 enriched upon IFN-β treatment of human iPSC-derived microglia, indicating that the

11 chemokine response to DNA damage mirrors type I interferon signalling. Furthermore, we find

12 that STING deletion leads to a defect in microglial chemotaxis under basal conditions and

13 upon ATM kinase loss. Overall, this work provides mechanistic insights into cGAS-STING-

14 dependent neuroinflammatory mechanisms and consequences of genome instability in the

15 central nervous system.

16 **INTRODUCTION**

17 Accumulation of DNA damage in the central nervous system (CNS) is commonly observed in

18 ageing and neurodegenerative diseases, including Alzheimer's and amyotrophic lateral

19 sclerosis[1–3]. Additionally, loss-of-function mutations in DNA damage response (DDR) genes

20 underpin neurodegeneration in monogenic disorders, such as ataxia with oculomotor apraxia

21 types 1-5 and ataxia-telangiectasia. Such vulnerability of the CNS to DDR defects is thought

22 to stem from the interplay between cell intrinsic effects of DNA damage on post-mitotic

23 neurons and glia as well as extrinsic signals resulting from glia-driven neuroinflammation[4,5].

24 One mechanism linking genome instability and neuroinflammation is the cytosolic DNA

25 sensing cGAS-STING pathway. Although responsible for mobilising antimicrobial responses

26 to cytosolic pathogenic DNA during infection, the cGAS-STING pathway can mount innate

27 immune responses to host DNA aberrantly localised in the cytosol following DNA damage[6].

28 The nucleotidyl transferase cGAS binds pathogenic double-stranded DNA (dsDNA) in the

29 cytosol, catalysing synthesis of 2',3'-cyclic GMP-AMP (cGAMP). cGAMP activates the

30 immune adaptor stimulator of interferon genes (STING) at the endoplasmic reticulum (ER),

31 inducing STING oligomerisation and translocation to the Golgi, where it recruits the TBK1

32 kinase and the interferon regulatory transcription factor IRF3. STING then acts as a platform

33 for TBK1 autophosphorylation at S172, as well as phosphorylation of STING at S366 and IRF3

34 at S396, culminating in nuclear translocation of IRF3. STING signalling also activates NF-κB,

35 leading to IRF3- and NF-κB-dependent transcription of type I interferons, interferon-stimulated

36 genes (ISGs), and pro-inflammatory cytokines which mount the antimicrobial response[7,8].

37 In the absence of infection, cytosolic accumulation of host DNA arising from genome instability

38 can also activate STING-dependent autoimmunity. One such example is cGAS activation by

39 nucleosome tethering at ruptured micronuclei, which can form during mitosis in cells

40 harbouring unresolved DNA damage[9–11]. Moreover, cGAS is activated by nuclear dsDNA,

41 RNA:DNA hybrids, telomeric DNA and mitochondrial DNA which can accumulate in the cytosol

42 following genotoxic or mitochondrial stress[12–15]. Thus, cGAS-STING promotes inflammation in

43 response to diverse self-DNA species.

44 In the brain, the strongest response to cGAS-STING activation occurs in microglia, the

45 resident macrophages of the CNS[16]. Microglia maintain CNS homeostasis via surveillance of

46 the microenvironment, phagocytosis of apoptotic cells and/or debris, synaptic pruning, and

47 production of neurotrophic factors[17–20]. During infection or injury, microglia can transition

48 towards a heterogenous 'reactive' state typified by enhanced phagocytosis, motility,

49 proliferation, and production of inflammatory mediators and reactive oxygen/nitrogen

50 species[21]. However, chronic microglial reactivity is implicated in neurodegenerative disease,

51 including those driven by genome instability, such as ataxia-telangiectasia (A-T)[5,22].

52 A-T is caused by loss-of-function mutations in ATM, a protein kinase which coordinates cellular

53 responses to cytotoxic DNA double strand breaks (DSBs) and oxidative stress. More broadly,

54 ATM preserves homeostasis by regulating redox balance, glucose metabolism, and

55 immunity[23]. In humans, A-T manifests as cerebellar degeneration and ataxia, and microglia-

56 driven neuroinflammation is increasingly implicated in disease phenotypes. We previously

57 demonstrated that ATM loss in human microglia-like cells activates RELB/p52 NF-κB

58 signalling and drives aberrant phagocytic activity, resulting in damage to the neuronal network

59 *in vitro*[24]. Furthermore, microglial activation is observed in Atm-deficient murine microglia and

60 correlates with motor neuron loss in the spinal cord of Atm-deficient rats[25–28]. Interestingly,

61 cerebellar microglia exhibit characteristics which may predispose them to exacerbated

62 immune responses to genome instability, including heightened immune vigilance and

63 enhanced proliferation[29,30]. Indeed, gene signatures enriched in cytosolic DNA sensing,

64 antiviral immunity, and proliferation are upregulated specifically in cerebellar microglia in A-T[31].

65 In addition, ATM deficiency activates cytosolic DNA sensing in diverse cell models, including

66 primary murine microglia and A-T patient-derived brain organoids[6,26,32–35]. STING activation in

67 ATM deficiency is also linked with neuronal damage via microglial secretion of IL-1β and

68 inflammatory responses mediated by senescent astrocytes[26,32]. However, the molecular

69 mechanisms of how STING signalling and type I interferon production shapes microglial

70 function in genome instability remain unclear.

71 Here, we investigate how loss of ATM kinase and persistent DNA damage regulate microglial

72 function. We find that genome instability drives chronic chemokine production in human

73 microglia-like cells and the chemokine response is regulated by the cGAS-STING pathway. In

74 agreement with this, bulk RNA-sequencing of iPSC-derived microglia treated with IFN-β

75 implicated type I interferon signalling in the governance of microglial migration. Indeed, we

76 find that STING deletion leads to defective microglial migration in basal conditions and upon

77 loss of ATM function. We propose that STING-mediated chronic chemokine production may

78 amplify neuroinflammation in genome instability via several different mechanisms, including

79 the recruitment of peripheral immune cells to the CNS and excessive energy expenditure.

80 Overall, this work provides mechanistic insight into STING-dependent regulation of microglial

81 function upon persistent DNA damage.

82

RESULTS

Loss of ATM function in human microglia-derived cells drives STING pathway activation and a type I interferon response

Individuals with classical A-T phenotypes typically possess nonsense mutations leading to complete loss of functional protein, STING signalling was therefore investigated in two monoclonal lines of *ATM* knockout (KO) human C20 microglia-like cells[24,36]. Loss of ATM function was confirmed by the lack of phosphorylation of the ATM substrate CHK2 T68 in response to camptothecin (CPT), a topoisomerase I inhibitor known to induce ATM activation (Supplemental Figure 1A and 1B)[37]. Increased phosphorylation of STING S366, TBK1 S172 and IRF3 S396 indicated that the STING pathway is activated in both *ATM* KO C20 lines (Figure 1A). Importantly, basal expression of *IFNB1* and the ISG *IFIT2* was induced in *ATM* KO cells, however, the induction in response to stimulation with the non-cyclic dinucleotide STING agonist, diABZI[38], was comparable to WT cells (Figure 1B).

To confirm whether loss of kinase activity induces phenotypes similar to loss of ATM protein, human microglia-derived HMC3 cells were treated with a selective ATM kinase inhibitor AZD1390 (ATMi)[39]. ATMi treatment blocked ATM auto-phosphorylation at S1981 and phosphorylation of CHK2 T68 in response to CPT, confirming successful kinase inhibition (Supplemental Figure 1C and 1D). ATMi also progressively increased levels of the DSB marker γH2AX, indicating accumulation of DNA damage (Supplemental Figure 1E and 1F). ATM inhibitor treatment led to a gradual increase in phosphorylation of STING, TBK1 and IRF3 between 3-9 days of treatment, and a concomitant upregulation of STING protein which at day 6, could be attributed to increased *STING1* transcription (Figure 1C and Supplemental Figure 1G). ATMi also induced nuclear translocation of IRF3 in a fraction of cells similar to that seen in diABZI-treated cells (Figure 1D and 1E). Low percentage of cells with nuclear IRF3 likely reflects that it can be difficult to detect owing to transient relocalisation[40]. Furthermore, ATM inhibition resulted in increased expression of the type I interferon, *IFNB1*, which was exacerbated upon stimulation with diABZI in ATMi-treated compared to control-treated HMC3 cells (Figure 1F). Different responses of ATMi-treated and *ATM* KO cells to additional stimulation with diABZI may reflect adaptation mechanisms following constitutive loss of ATM, compared to the short-term loss of function upon kinase inhibition. Taken together, these data confirm that loss of ATM function leads to activation of STING and a type I interferon response in human microglia-like cells.

Loss of ATM function leads to cGAS accumulation at micronuclei

Micronuclei are a hallmark of genome instability known to induce cGAS-STING activation in proliferating cells[9,10]. Although microglial turnover is low in the healthy CNS, microglial proliferation can be stimulated in response to perturbations in their microenvironment. For example, rapid expansion of the population of microglia is observed following their depletion with CSF1R inhibitors in mice and in mouse models of neurodegenerative prion disease[41,42]. Moreover, cell cycle genes are upregulated in cerebellar microglia in A-T, suggesting an increase in proliferative capacity[31].

To confirm that loss of ATM function induces the formation of micronuclei, human microglia-like HMC3 cells were treated with ATMi for 6 days followed by drug washout for 4 days (Figure 2A). As expected, loss of ATM activity led to a significant increase in micronucleated cells, which was rescued by inhibitor washout (Figure 2B and 2C). Similarly, *ATM* KO C20 lines displayed an increased micronuclei frequency compared to wild-type (WT) cells (Figure 2D and 2E). This increase was less marked than that seen with kinase inhibition, likely due to the exacerbated genome instability caused by loss of kinase activity relative to loss of ATM protein[43,44].

Since cGAS can accumulate at micronuclei following micronuclear envelope collapse[9,10], its localisation was determined in ATMi-treated HMC3 cells by immunofluorescence using a cGAS-specific antibody (Figure 2F and Supplemental Figure 2A). The number of cGAS-positive micronuclei significantly increased upon ATMi treatment as compared to control (Figure 2G). An increase in the number of cGAS-positive micronuclei was also observed in *ATM* KO C20 lines, confirming that cGAS accumulates at micronuclei in ATM-deficient human microglia-like cells (Figure 2H). However, ATM inhibition or deletion did not affect the proportion of cGAS-positive micronuclei, indicating that loss of ATM function does not alter the propensity for micronuclear envelope collapse or cGAS recruitment (Supplemental Figure 2B and 2C). Collectively, these data confirm that micronuclei are a source of cytosolic DNA in ATM-deficient microglia-like cells.

ATM loss reportedly induces accumulation of cytosolic DNA fragments and leakage of mtDNA in some cell types[6,26,33,35]. As cGAS senses dsDNA[45], dsDNA localisation was visualised in ATMi-treated HMC3 cells by immunofluorescence confocal microscopy. Co-staining for the mitochondrial marker TOM20 confirmed that cytosolic dsDNA did not localise to the mitochondria, and loss of dsDNA signal following DNase I treatment confirmed antibody specificity. However, no increase in cytosolic dsDNA was observed upon ATM inhibition (Supplemental Figure 2D and 2E). One reported mechanism of mtDNA leakage in

6

149   ATM-deficient murine cancer cells is via downregulation of the mitochondrial transcription

150   factor A (TFAM)[33]. However, *TFAM* mRNA levels were unchanged in ATMi-treated HMC3

151   cells, in line with reports in Atm-deficient mouse thymocytes (Supplemental Figure 2F)[46].

152   These results indicate that cGAS-STING activation likely originates primarily from micronuclei

153   formation.

154   To address the requirement for cell cycle progression in activating STING, mitotic entry was

155   blocked using the CDK1 inhibitor (CDK1i) RO-3306 in the absence or presence of ATMi. Cells

156   were treated with ATMi for 6 days, with addition of CDK1i for the final 48 h (Supplemental

157   Figure 2G). Immunoblotting and cell cycle analysis confirmed effective ATM inhibition and

158   synchronisation of HMC3 cells in G2 phase upon CDK1i treatment (Supplemental Figure 2H

159   and 2I). ATM-inhibitor induced phosphorylation of STING and IRF3 and increased expression

160   of the interferon-responsive transcription factor STAT1 were alleviated by CDK1i treatment,

161   confirming a requirement for mitotic progression (Supplemental Figure 2J). Notably, TBK1

162   protein levels are mildly downregulated in synchronised cells which may partially contribute to

163   pathway inhibition. This downregulation may be linked with previously reported roles for TBK1

164   in the G2/M checkpoint and microtubule dynamics during mitosis[47,48].

165   Taken together, these data indicate that loss of ATM function in proliferating microglia leads

166   to recognition of micronuclei by cGAS, providing a source of sterile STING-dependent

167   inflammation.

168   **cGAS dependency of STING activation**

169   STING activation can occur through mechanisms independent of cGAS and cytosolic DNA,

170   such as inappropriate trafficking to the Golgi or via nuclear signalling upon sensing of DNA

171   damage by PARP1[49,50]. Furthermore, ATM inhibition was reported to activate TBK1 in a

172   cGAS-STING-independent manner via SRC kinase in pancreatic cancer cells[34].

173   To confirm whether interferon signalling is activated via canonical cytosolic DNA sensing,

174   cGAS and STING were depleted using siRNA in ATMi-treated HMC3 microglia. Knockdown

175   (KD) of cGAS abolished phosphorylation of STING following ATMi treatment, while KD of

176   cGAS or STING abolished TBK1 phosphorylation (Figure 3A and Supplemental Figure 3A).

177   Biochemical fractionation revealed that nuclear translocation of phosphorylated IRF3 and

178   STAT1 in ATMi-treated cells was abolished upon cGAS or STING KD (Figure 3B and

179   Supplemental Figure 3B). Importantly, an increase in expression of *IFNB1* and *IFIT2* in

180   ATMi-treated cells is abolished upon cGAS or STING KD, while induction of *IL6* is only partially

181   dependent on cGAS and STING (Figure 3C). As *IL6* is a target of NF-κB transcription factors,

7

182 and we previously reported activation of non-canonical NF-κB upon loss of ATM function,

183 residual inflammatory signalling upon cGAS-STING deletion may be driven by this pathway[24].

184 Taken together, these data demonstrate that canonical cGAS-STING signalling drives the type

185 I interferon response in ATM-deficient microglia-derived cells.

186 **Type I interferon signalling elicits chemokine and motility transcriptional programmes**

187 **in human iPSC-derived microglia**

188 STING signalling has been linked with activation of NF-κB signalling and induction of

189 senescence programmes in Atm-deficient murine microglia and A-T brain organoids[26,32].

190 However, type I interferon is a major arm of transcriptional responses downstream of

191 mammalian STING[51]. To determine how type I interferon shapes microglial function, bulk

192 RNA-sequencing (RNAseq) was performed in human iPSC-derived iCell microglia treated with

193 human IFN-β for 6 or 24 h (Figure 4A). As expected, differentially expressed genes (DEGs) in

194 IFN-β-treated iPSC-derived microglia are enriched in gene ontology (GO) biological processes

195 associated with antiviral immunity, including positive regulation of immune response, response

196 to virus and positive regulation of inflammatory response (Figure 4B). Importantly, GO terms

197 associated with cell locomotion, motility and migration were among the top 5 enriched

198 processes. Processes linked with actin filament organisation, cell polarity and cell shape also

199 featured in the top 20 enriched GO processes.

200 The chemokine superfamily is divided into C, CC, CXC, and CX3C subtypes based on the

201 amino acid arrangement between conserved N-terminal cysteine residues. Chemokines signal

202 via transmembrane G-protein coupled receptors (GPCRs) to regulate cell polarity, cytoskeletal

203 organisation and adhesion, driving cell recruitment along a chemotactic gradient[52]. Protein

204 interaction network analysis at 6 and 24 h identified a significant cluster of chemokines and

205 their receptors, indicating enrichment of microglial chemokine signalling following IFN-β

206 treatment (Figure 4C). Specifically, *CXCL9*, *CXCL10* and *CXCL11,* ligands of the CXCR3

207 receptor, and *CCL8*, a ligand of CCR2, are among the top upregulated chemokines upon

208 IFN-β treatment at both 6 and 24 h (Figure 4D). In addition, *CCL5* among other chemokines

209 of the CC family, is highly upregulated (Figure 4C and 4D). Therefore, chemokine signalling

210 is a critical outcome of type I interferon responses in human microglial cells.

211 **ATM loss drives STING-dependent chemokine production in microglia-derived cells**

212 Given the induction of chemokine and cell motility programmes in response to IFN-β treatment

213 in iPSC-derived microglia, we sought to investigate whether ATM loss induces microglial

214 chemokine production and whether this could be STING dependent. Single-cell RNAseq

8

215 previously identified *Cxcl10* and *Ccl5* as signature ISGs induced specifically in micronucleated

216 cells[10], therefore mRNA levels of these chemokines were assessed in ATM-deficient

217 microglia-like cells. *CCL5* and *CXCL10* were found to be significantly upregulated in *ATM* KO

218 C20 cells and induced by STING activation with diABZI (Figure 5A). As siRNA delivery and

219 lipofection can activate the innate immune system[53,54], *STING1* KO HMC3 cells were

220 established to further investigate the consequences of chronic STING activation on microglial

221 function. In two monoclonal *STING1* KO lines, TBK1 S172 and IRF3 S396 phosphorylation

222 was abolished (Supplemental Figure 4A and 4B) and perinuclear STING clusters were no

223 longer detectable in response to diABZI, confirming the lack of functional STING

224 (Supplemental Figure 4C).

225 We therefore focused on the role of STING in chemokine production in basal conditions and

226 upon treatment of WT and *STING1* KO HMC3 cells with ATMi (Figure 5B). As expected, the

227 induction of *IFNB1* in cells treated with ATMi or diABZI was completely abolished in *STING1*

228 KO lines (Supplemental Figure 4D). Although *IFNB1* mRNA was induced, ATM inhibition

229 increased secretion of IFN-α2a rather than IFN-β, and this was dependent on STING

230 (Supplemental Figure 4E). This discordance between mRNA levels is likely to be attributed to

231 the kinetics of the secretory response. Importantly, ATM inhibition also induced a robust

232 chemokine response, evidenced by increased mRNA levels of *CCL5* and *CXCL10*, which were

233 fully dependent on STING. Stimulation with diABZI similarly induced *CCL5* and *CXCL10*

234 expression (Figure 5C). Moreover, *STING* deletion markedly reduced *CCL5* mRNA in basal

235 conditions, and a similar tendency was observed in the case of *CXCL10*, suggesting tonic, i.e.

236 basal, STING-dependent chemokine signalling. As *CXCL10* was the most strongly

237 upregulated gene following IFN-β treatment in iPSC-derived microglia, its concentrations were

238 measured in cell culture supernatants. ATM inhibition promoted CXCL10 secretion in a

239 STING-dependent manner, whereas CXCL10 was not detected in supernatants from *STING1*

240 KO cells (Figure 5D).

241 Given the robust chemokine response *in vitro*, mRNA levels of *CGAS, STING1, CCL5* and

242 *CXCL10* were determined by RT-qPCR in cerebellar homogenates from individuals with A-T

243 and from age- and gender-matched individuals with no known diseases of the CNS (Figure

244 5E and 5F). Confirming previous single-nucleus RNAseq data, expression of *CGAS* and

245 *STING1* was significantly upregulated in A-T cerebella compared to matched controls[31].

246 Importantly, levels of *CCL5* and *CXCL10* were also increased in A-T brains, albeit not

247 significantly, likely owing to genetic variability between individuals and a small sample size

248 limited by tissue availability (Figure 5F). Whole cerebellum gene expression changes therefore

249 indicate upregulation of *CGAS, STING1,* and possibly chemokines in A-T. Taken together,

250 these data demonstrate that STING drives production of chemokines upon loss of ATM

251 function in human microglia-like cells with potential relevance in human disease.

252 **Persistent DNA damage promotes a STING-dependent chemokine response**

253 To investigate the role of DNA damage in STING-dependent chemokine responses, WT and

254 *STING1* KO HMC3 cells were treated with the topoisomerase II poison etoposide, the DNA

255 synthesis inhibitor aphidicolin and the DNA crosslinking agent mitomycin C. To model

256 persistent low-level DNA damage, cells were treated for 6 days using low doses of drugs that

257 did not induce cell death (Supplemental Figure 5A). All DNA damaging agents induced the

258 formation of micronuclei and consequent STING activation, as evidenced by increased STING

259 S366 and TBK1 S172 phosphorylation, which was absent in *STING1* KO cells (Supplemental

260 Figure 5B and 5C). Moreover, all three agents induced *CCL5* expression, which was

261 dependent on STING (Supplemental 5D). These data indicate that DNA damage, rather than

262 ATM loss per se, drives STING-dependent chemokine induction in human microglia-derived

263 cells.

264 **ATM inhibition drives microglial chemotaxis in a STING-dependent manner**

265 Microglia are highly motile cells, as their processes dynamically survey their microenvironment

266 in the absence of a stimulus, and are rapidly directed towards sites of infection or injury[55].

267 Given that STING regulates tonic chemokine production in microglia-like cells, the role of

268 STING in regulating basal microglial migration was investigated. To address this, a variant of

269 the scratch-wound assay was utilised, in which cells are seeded in a well containing silicone

270 inserts which are subsequently removed to produce a uniform cell-free gap (Figure 6A). Live

271 cell imaging showed that deletion of *STING1* leads to delayed gap closure, indicating that

272 STING regulates basal microglial migration (Figure 6B and 6C). Furthermore, chemotactic

273 migration of WT and *STING1* KO HMC3 cells, which were grown in the presence or absence

274 of ATM inhibitor for 6 days, was investigated using xCELLigence label-free real-time cell

275 analysis based on measuring cellular impedance (Figure 6D)[56]. Loss of ATM activity was

276 demonstrated to enhance chemotactic migration of cells towards their respective conditioned

277 medium, and this effect was reduced in the absence of STING (Figure 6E).

278 Overall, these data demonstrate that STING regulates chemotaxis of microglia-derived cells

279 in basal conditions and following loss of ATM function.

280

DISCUSSION

In this study, we utilised A-T as a model genome instability disorder to explore how cGAS-STING signalling regulates microglial function upon persistent DNA damage. In line with previous observations upon ATM deletion or pharmacological inhibition, we find that the cGAS-STING pathway induces chronic inflammation following ATM loss in models of human microglia-derived cells[6,26,32,35]. Both genomic and mitochondrial origins of cytosolic DNA in ATM deficiency have previously been proposed[12,33,35]. Whilst a mitochondrial origin cannot be ruled out in the present work, we find that STING signalling in the absence of ATM is associated with cGAS activation by micronuclei in proliferating microglia (Figure 7). Indeed, ATM-deficient cells present with chromosomal rearrangements that form upon non-homologous end joining of single-ended DSBs and could drive micronucleus formation[57]. Evidently, STING-dependent inflammation is phenocopied upon prolonged treatment of ATM-proficient microglia-derived cells with a range of DNA damaging agents, all of which could potentiate the formation of DSBs and consequently micronuclei. These observations argue against a specific effect of ATM loss as a driver of STING activation in microglia. We therefore propose that chronic inflammation in ATM deficiency is driven by genome instability, in line with the nuclear origin of cytosolic DNA upon Atm inhibition in murine microglia[12].

As micronuclei form during mitosis, the cellular proliferative capacity will dictate the rate of micronuclei formation. Importantly, microglial proliferation is highly responsive to external cues, including inflammation, and expansion of the microglial compartment is frequently observed in neurodegenerative disease[41,58]. It is therefore possible that microglial proliferation is stimulated by perturbations in the CNS microenvironment during genome instability, perpetuating neuroinflammatory processes. Consistent with this, microgliosis is observed in the spinal cord of Atm-deficient rats and several studies have highlighted increased turnover of cerebellar microglia relative to cortical microglia, suggesting a region-specific increase in microglial proliferative capacity[25,30,31].

Previous studies established a connection between genome instability, activation of STING, and inflammation in ATM deficiency[12,26,32,35]. We extend these findings by demonstrating that interferon responses to ATM inhibition are abolished in STING-deficient cells, however, the consequences of type I interferon production on microglial homeostasis are unclear. We therefore focus on investigating interferon-dependent regulation of microglial function. In line with IFN-α administration in murine microglia, we discover that IFN-β potently upregulates signalling networks associated with chemotaxis and migration in human iPSC-derived microglia[59,60]. These data identify chemotactic responses as a key outcome of type I interferon signalling. Indeed, STING signalling induces production of chemokines, such as *CCL5* and

316   *CXCL10*, in human microglia-like cells upon ATM loss or persistent DNA damage (Figure 7).
317   Whilst acute chemotactic responses are critical for antimicrobial immunity, excessive and/or
318   chronic production of chemokines is implicated in detrimental microglial functions *in vivo*. For
319   example, CXCL10-CXCR3 signalling regulates microglial recruitment and dendritic loss
320   following axonal injury[61]. Moreover, microglia-derived CCL3/4/5 activates neuronal CCR5,
321   leading to autophagy inhibition and accumulation of protein aggregates in mouse models of
322   Huntington's disease and tauopathy[62]. Interestingly, CCR5 also promotes microglial
323   recruitment to cerebral vasculature to support the blood brain barrier (BBB) during acute
324   inflammation, however, chronic inflammation drives BBB dysfunction via microglial
325   phagocytosis of astrocytic end feet[63]. Sustained, excessive chemokine production may
326   therefore shift the balance towards eliciting deleterious effects on neuronal function and the
327   CNS microenvironment. As chemokines are implicated in recruitment of peripheral immune
328   cells, the question of whether cGAS-STING signalling drives immune infiltration during chronic
329   CNS inflammation in A-T warrants further investigation[64].

330   Importantly, this study identifies STING as a regulator of microglial chemotaxis, both in basal
331   conditions and during ATM deficiency (Figure 7). In mice, STING activation mediates
332   chemotactic recruitment of T-cells into the inflamed peritoneum and tumour-infiltrating
333   neutrophils[65,66]. Conversely, STING activation supresses migration of cancer cells and tumour-
334   infiltrating neutrophils by reducing translation of the matrix-remodelling serine peptidase
335   PLAU[67]. However, knowledge of whether STING regulates microglial migration is lacking. We
336   find that STING-deficient microglia-like cells display a marked defect in migration in the
337   absence of stimulation. Whilst STING may act intrinsically to regulate cytoskeletal dynamics,
338   it is possible that tonic chemokine signalling underlies this phenotype, as STING loss reduced
339   basal chemokine expression. Previous work identified enhanced migration in Atm-deficient
340   primary murine microglia and astrocytes isolated from the cerebellum, but not the cerebral
341   cortex[27]. This indicates cerebellum-specific effects of ATM loss on microglial migration may
342   exist, and we propose that STING signalling may underlie this process. In addition, the Rho
343   family of small GTPases coordinate actin cytoskeleton dynamics during cell migration. In ATM-
344   deficient human fibroblasts, oxidative stress reportedly promotes increased migration by
345   activating the Rho GTPase Rac1, suggesting that oxidative stress may also factor into
346   regulation of cell migration upon ATM loss[68].

347   Microglial soma are largely immobilised during baseline microglial motility *in vivo*, however,
348   their processes are highly motile enabling constant surveillance of the local parenchyma[55].
349   Uniquely, cerebellar microglia exhibit baseline soma motility and frequently interact with
350   Purkinje cell soma and dendrites[69]. Enhanced sampling of the surrounding parenchyma may
351   improve scavenging of apoptotic cells or debris and detection of pathogenic stimuli, promoting

352   beneficial outcomes in an acute setting. Conversely, increased surveillance in the

353   degenerating brain may amplify recognition of neuronal stress, including via chemotactic-

354   driven clustering of activated microglia, which might potentiate detrimental functions of

355   microglia. For example, we previously showed that ATM-deficient microglia form clusters

356   which damage neurons *in vitro* through aberrant engulfment[24]. Finally, cytoskeletal

357   reorganisation required for sustained chemotaxis is energetically expensive and may drive

358   metabolic reprogramming and microglial dysfunction.

359   In conclusion, this study identifies cytosolic DNA sensing as a critical mechanism regulating

360   microglial motility and chemotaxis in health and disease. Given the expanding roles of cGAS-

361   STING signalling in neurodegeneration[70], our study uncovers mechanistic insights into

362   inflammatory mechanisms not just in A-T, but more broadly in neurological diseases

363   associated with genome instability and excessive interferon production in the CNS. This work

364   therefore provides a rationale for exploring STING inhibition as a therapeutic strategy to

365   alleviate neurological decline in A-T and similar genome instability disorders.

MATERIALS AND METHODS

Cell culture

368   Immortalised foetal human microglial HMC3 cells were kindly gifted by Dr Brian Bigger,

369   University of Manchester[71]. HMC3 cells were maintained in DMEM (4.5 g/L glucose,

370   GlutaMAX™ supplement, no pyruvate; Gibco™) supplemented with 10% (v/v)

371   heat-inactivated FBS (HI-FBS; Gibco). Immortalised adult human C20 microglial cells were

372   kindly provided by Dr David Alvarez Carbonell, Case Western Reserve University[72]. C20 cells

373   were cultured in DMEM:F-12 with 3.151 g/L glucose, L-glutamine and 15 mM HEPES (Merck)

374   supplemented with 1% (v/v) HI-FBS and N-2 supplement (Gibco™). *ATM* knockout (KO) C20

375   cells generated using CRISPR-Cas9 were described previously[24].

376   All cell lines were cultured at 37°C in 5% CO_2 and 95% humidity. Cells were routinely tested

377   for mycoplasma and experiments were performed below passage 35.

Generation of *STING1* KO HMC3 cells

379   *STING1* KO HMC3 cells were generated using the pSpCas9(BB)-2A-Puro (PX459) V2.0

380   vector kindly gifted by Feng Zhang (Addgene plasmid #62988)[73] containing the following single

381   guide RNA (sgRNA) sequence targeting *STING1*: 5'-GCTGGGACTGCTGTTAAACG-3'. The

382   vector was delivered into HMC3 cells by Magnetofection™ using Glial-Mag (Oz Biosciences)

383   according to manufacturer's instructions. Cells were then selected with 1.2 µg/mL puromycin

384   for 3 days before single cell cloning.

385   Clones were screened by fluorescent PCR-capillary electrophoresis. DNA was extracted from

386   clones using QuickExtract™ DNA Extraction Solution (Lucigen) according to the

387   manufacturer's protocol. A region flanking the sgRNA target site was amplified using a 5'-FAM

388   labelled forward primer (5'-FAM-GCTAGGCATCAAGGGAGTGA-3') and unlabelled reverse

389   primer (5'-TGGATTTCTTGGTGCCCACA-3'). PCR was performed using Phusion polymerase

390   (Invitrogen) with the following cycling parameters: denaturation (98ºC, 30 s); 35 cycles of

391   denaturation (98ºC, 10 s), annealing (62ºC, 30 s) and extension (72ºC, 15 s); final extension

392   (72ºC, 5 min). Fragment analysis was performed by capillary electrophoresis on a 3100 XL

393   Genetic Analyser (Life Technologies) by the Department of Biochemistry sequencing facility

394   (University of Cambridge, UK). Successful KO of *STING1* was confirmed by Sanger

395   sequencing and western blotting.

396   **RNA interference**

397   siRNA duplexes were synthesised by Merck and used at a final concentration of 25 nM unless

398   stated otherwise (sequences are listed in Supplemental Table 1). siRNA was delivered by

399   forward transfection using Lipofectamine® RNAiMAX™ Transfection Reagent (Invitrogen™)

400   according to manufacturer's instructions. Media was changed 8 h post-transfection to limit

401   toxicity and cells were harvested 72 h post-transfection.

402   **Chemical treatments**

403   The ATM inhibitor AZD1390 (ATMi; Selleck Chemicals) was used at 10 nM for 1 – 9 days with

404   replenishment of the inhibitor every 2 days. To induce ATM activation, cells were treated with

405   1 µM camptothecin (CPT; Cayman Chemical Company) for 1 h. The STING agonist diABZi

406   (Selleck Chemicals) was used at 1 µM. To induce DNA damage, cells were treated with

407   250 nM Etoposide (ETO; Cayman Chemical Company), 30 nM Mitomycin C (MMC; Santa

408   Cruz), or 150 nM Aphidicolin (APH; Merck) for 6 days. To induce apoptosis, cells were treated

409   with 1 µM staurosporine for 6 h. Treatment times are indicated in figure captions. For

410   compounds dissolved in DMSO, DMSO concentration was equivalent between conditions and

411   <0.1% (v/v).

412   For 2',3'-cGAMP stimulation, cells were washed in PBS then incubated for 3 min at 37ºC in

413   digitonin permeabilization buffer (50 mM HEPES pH 7.0, 100 mM KCl, 3 mM MgCl$_2$,

414   0.1 mM DTT, 85 mM sucrose, 0.2% (w/v) BSA, 1 mM ATP, 0.1 mM GTP, 4 µM digitonin) with

415   or without 7 µM 2',3'-cGAMP (Invivogen). Cells were further washed in PBS and incubated in

14

416   culture medium until collection. Incubation times post-treatment are indicated in figure
417   legends.

Cell synchronisation in G2 cell cycle phase

419   Exponentially growing cells were pre-treated with 10 nM ATMi or DMSO as a control for 24 h,
420   then treated for an additional 24 h in the presence (synchronised in G2 cell cycle phase) or
421   absence (asynchronised) of 9 μM CDK1 inhibitor RO-3306 (CDK1i; Tocris Bioscience) prior
422   to collection.

Cell cycle analysis

424   Cells were pulsed with 10 μM BrdU for 30 min, then collected by trypsinisation and fixed in
425   ice-cold 70% ethanol for at least 30 min. After removal of ethanol by centrifugation, cells were
426   incubated in 2 M HCl containing 0.1 mg/mL pepsin for 20 min at 37ºC. Cells were washed
427   several times in PBS and 1% (v/v) HI-FBS in PBS, collected by centrifugation at 350 g for
428   5 min and incubated with anti-BrdU antibody at 1:100 dilution in 1% (v/v) HI-FBS-PBS for 1 h
429   at 22ºC. Cells were washed in PBS and incubated with AlexaFluor 488 goat anti-mouse
430   secondary antibody diluted 1:200 in 1% (v/v) HI-FBS-PBS for 45 min at 22ºC. Samples were
431   further treated with 100 μg/mL RNase A (QIAGEN) for 30 min at 37ºC, supplemented with
432   100 ng/mL propidium iodide (PI) and analysed on the green FL1-A and red FL2-A channels
433   using an Accuri™ C6 Plus flow cytometer (BD Biosciences).

Preparation of whole cell lysates

435   Cells were lysed in ice-cold RIPA buffer (25 mM Tris-HCl, pH 8.0, 150 mM NaCl, 1% (v/v)
436   Triton X-100, 1% (w/v) sodium deoxycholate, 0.1% (w/v) sodium dodecyl sulphate (SDS),
437   5 mM EDTA) supplemented with 1 mM phenylmethylsulfonyl fluoride, 1 μM staurosporine,
438   1 μg/mL each of aprotinin, chymostatin, leupeptin, pepstatin, N-ethylmaleimide and
439   1x phosphatase inhibitor cocktail (Calbiochem). Lysates were incubated with rotation for
440   30 min at 4ºC and centrifuged at 20,000 g for 20 min at 4ºC. The protein concentration of
441   supernatants was measured using Bradford assay reagent (Bio-Rad). Lysates were prepared
442   at equal concentrations and boiled at 95ºC for 10 min in denaturing loading buffer
443   (25 mM Tris-HCl, pH 6.8, 2.5% v/v β-mercaptoethanol, 1% (w/v) SDS, 5% (v/v) glycerol,
444   0.05 mg/mL bromophenol blue, 1 mM EDTA) before SDS-PAGE.

Biochemical fractionation

Cell pellets were harvested by trypsinisation and resuspended in plasma membrane lysis buffer (20 mM Tris-HCl, pH 7.4, 2.5 mM $MgCl_2$, 0.3% (v/v) NP-40) supplemented with protease/phosphatase inhibitors as above. After incubation on ice for 15 min, lysates were centrifuged for 10 min at 1,500 g, 4ºC. The supernatant served as the cytoplasmic fraction and the pellet containing nuclei was resuspended in 20 mM phosphate buffer, 0.5 M NaCl, 1 mM EDTA, 0.75% (v/v) Triton X-100, glycerol 10% (v/v) and 5 mM $MgCl_2$. After incubation on ice for 15 min, nuclear lysates were centrifuged for 10 min at 20,000 g to obtain the nuclear fraction. The protein content of cytosolic fractions was determined by Bradford and equal volumes of cytoplasmic and nuclear fractions were analysed by SDS-PAGE.

Immunoblotting

Proteins were separated using 10 or 4-16% Tris-glycine SDS-PAGE and transferred onto Immobilon®-FL PVDF membranes, which were blocked using Intercept®-TBS blocking buffer (LI-COR Biosciences). Primary antibodies were diluted in Intercept®-TBS, 0.1% (v/v) Tween®20 and secondary antibodies were diluted in Intercept®-TBS, 0.1% (v/v) Tween®20, 0.01% (w/v) SDS. Antibodies are detailed in Supplemental Table 1. Membranes were visualized using an Odyssey® CLx Imaging System and quantification was performed using Image Studio™ Lite Software (both LI-COR Biosciences). Band intensities were normalised to loading controls, or to the corresponding total protein for phosphorylated proteins, and presented as fold-change relative to the experimental control. Immunoblots are representative of at least 3 independent experiments.

Brain tissue homogenisation and processing

Blocks of fresh frozen cerebellar tissues from individuals with A-T and that of individuals with no known diseases of the CNS (controls) were obtained from the NIH Neurobiobank at the University of Maryland, Baltimore, MD (United States). The use of samples was covered by the University of Maryland's IRB approval no. HP-00042077 and the HTA site license no. 12196 that permits work with human tissue at the Department of Biochemistry (University of Cambridge, UK). The A-T and control tissue pairs were matched by age and gender (Supplemental Table 2). The tissues were cut into 20-μm thick sections with a cryostat (Leica CM 1950) maintained at -20ºC. To extract the RNA, 5-6 sections were collected into a tube containing lysing matrix beads (1.4 mm ceramic spheres, MP Biologicals), supplemented with 1 mL of the TRI Reagent® (Merck), and snap frozen on dry ice. After thawing, samples were homogenized by vortexing and the RNA was extracted as previously described[74].

16

478   To extract proteins, tissue sections were collected into tubes with lysing matrix beads (as
479   above) containing RIPA buffer supplemented with protease/phosphatase inhibitors as above
480   and snap frozen in liquid nitrogen. After thawing on ice, tissues were homogenized by
481   intermittent vortexing at 4ºC, then centrifuged at 20,000 g for 20 min at 4ºC. Protein lysate
482   concentrations were measured and prepared for SDS-PAGE analyses as above.

483   **RT-qPCR**

484   Total RNA from adherent cells was extracted using the RNeasy Mini Kit (QIAGEN) and treated
485   with DNase I (ThermoFisher) according to manufacturer's instructions. RNA integrity was
486   assessed by agarose gel electrophoresis and purity was determined by measuring the ratio of
487   absorbance at 260/280 ($A_{260/280}$) and 260/230 ($A_{260/230}$) using a NanoDrop™ ND-1000
488   Spectrophotometer (ThermoFisher Scientific). RNA with intact 28S and 18S ribosomal RNA
489   bands at a ratio of approximately 2:1 with $A_{260/280}$ of ~2 and $A_{260/230}$ of 1.8 – 2.2 was used for
490   reverse transcription (RT). When tissues were used as a source, the integrity of
491   DNAse I-treated RNA was determined using the Agilent RNA 6000 Pico Kit and an Agilent
492   2100 Bioanalyzer (Agilent Technologies). RNA with RIN values > 4 was used for RT.

493   RT was performed with 400 ng RNA per 20 µL reaction using the qPCR cDNA Synthesis Kit
494   (PCR Biosystems). cDNA was treated with RNase H (New England Biolabs) for 20 min at
495   37ºC and diluted 1:5 prior to qPCR.

496   Primers for qPCR were synthesised by Merck and used at 200 nM final (sequences in
497   Supplemental Table 1). Primer efficiencies were assessed by standard curve and specificity
498   was confirmed by melt curve analysis and agarose gel electrophoresis. qPCR was performed
499   using 2x qPCR BIO SyGreen Blue Mix Lo-ROX (PCR Biosystems) in triplicate 10 µL reactions
500   in 384-well plates (Applied Biosystems). Amplification was performed on a QuantStudio™5
501   Real-Time PCR System (ThermoFisher Scientific) using the following cycling parameters:
502   initial denaturation and polymerase activation at 95ºC for 2 min; 40 cycles of 95ºC for 5 s and
503   60ºC for 30 s, and a subsequent melt step: 95ºC for 15 s, 60ºC for 60 s, 95ºC for 15 s.

504   Data was analysed using the QuantStudio™ Design & Analysis Software. Mean C_q values of
505   technical triplicates were normalised to the reference genes *RPS13* or *IPO8* and experimental
506   controls using the δδC_q method[75]. Data is presented as average $\log_2$ fold-change ± SD except
507   for *TFAM* mRNA, which is presented as fold change, and human tissue data, which is
508   presented as $2^{-\delta C_q}$.

RNAseq of IFN-β treated human iCell microglia

iCell human microglia (FujiFilm CDI) were derived from peripheral blood mononuclear cells from a donor with no known disease phenotypes. 3 independent vials of iCell microglia were seeded at 5×10^4 cells per well across 3 independent 96-well plates and treated the following day with vehicle or 5 ng/mL human IFN-β (R&D Systems). Cells were treated for 6 or 24 h prior to collection and stored at -80ºC prior to RNA extraction.

For cell lysis, RNAdvance Cell v2 (Beckman Coulter) was added to iCell Microglia in 96-well plates on dry ice. Plates were warmed to room temperature, treated with Proteinase K and cells were lysed by gentle pipetting followed by incubation at room temperature for 30 min. RNA extraction was performed according to manufacturer's protocol on a Biomek i7 Hybrid robotic workstation (Beckman Coulter). mRNA enrichment and sequencing library preparation was performed using KAPA mRNA HyperPrep Kit (Roche) according to the manufacturer's protocol on a Tecan Fluent® liquid handler. Library quality was assessed on a fragment analyser instrument using SS NGS fragment kit (1-6,000 bp; Agilent). Sequencing was performed on NovaSeq 6000 platform using a 200 cycles SP Reagent Kit v1.5 (both Illumina) at a loading concentration of 1.85 nM. Sequencing generated 194.6 Gb of data with Q30 of over 91.6%. The data will be deposited in the NCBI Sequence Read Archive (SRA) and referenced upon acceptance of the manuscript (currently available on request).

Transcriptomics data analysis

FastQC files were generated and trimmed with TrimGalore[76] and quality review was performed by FastQC[77] before and after quality trim. Reads were aligned with STAR aligner (version 2.6.1d, using the default settings) to the HG38 human genome and ENSEMBL94 annotation GTF file. After alignment and summarization with featureCounts of the Subread package (feature Counts release 1.6.3 and picard version 2.18.21), samples were normalized using voom (limma package) and differential gene expression analysis was carried out with limma implemented in R. FDR adjusted p-value < 0.05 was used as the cut-off (Benjamini-Hochberg method). Gene annotations were obtained by biomaRt.

Pathway and network analyses

For protein interaction network analysis and visualization Cytoscape was used (version 3.8.0) and the StringApp plugin using a confidence score cutoff of 0.7 (high confidence)[78,79]. Gene Ontology (GO) and KEGG database enrichment was performed using R and the clusterProfiler package with an adjusted p-value cutoff of 0.05[80].

Measurements of cytokine/chemokine secretion

Following 72 h pre-treatment with 10 nM AZD1390 or DMSO as a control, WT and *STING1* KO HMC3 cells were seeded at a density of 21,000 cells/cm^2 in 6-well plates. After 48 h, cells were washed in PBS and placed in DMEM supplemented with 0.5% (v/v) HI-FBS. Cells were stimulated with 1 µM diABZi for 24 h prior to collection. Conditioned medium was centrifuged at 400 *g* for 10 min at 4ºC to pellet cells and debris, then snap frozen on dry ice and stored at -80ºC until use. After collection of medium, remaining cells were lysed in RIPA buffer and total protein content was measured by Bradford assay. The overall protein content was comparable between treatments.

Secretion of IFN-α2a, IFN-β, and CXCL10 was measured using a Mesoscale Discovery (MSD) U-PLEX assay following the manufacturer's protocol. Plates were read on a MESO SECTOR S 600 (MSD) and data was analysed using MSD Discovery Workbench (version 4).

Immunofluorescence

Cells were seeded on glass coverslips and fixed in 4% (w/v) paraformaldehyde for 15 min at room temperature. Coverslips were then permeabilised with 0.2% (v/v) Triton X-100 for 10 min and blocked in 3% (w/v) BSA, 0.05% (v/v) Tween®20, 0.3 M glycine in PBS for 1 h. For detection of IRF3, coverslips were fixed and permeabilised in ice-cold methanol for 5 min before blocking. Antibodies were diluted in blocking buffer (Supplemental Table 1) and cells were incubated with primary antibodies at 4ºC overnight in a humidified environment. Coverslips were then washed in PBS with 0.1% (v/v) Tween®20 (PBST) and incubated with secondary antibodies for 45 min at room temperature. Coverslips were washed in PBST before mounting onto glass slides using Fluoroshield™ mounting medium (Merck) supplemented with 1.5 µg/mL DAPI.

Detection of cytosolic dsDNA was performed as previously described with amendments[81]. Coverslips were PFA-fixed and permeabilised with 0.2% (v/v) Triton X-100 for 5 min at 4ºC. To remove cytosolic RNA, coverslips were treated with 2 mg/ml RNase A (QIAGEN) for 30 min at 37ºC, then washed in PBS. Antibody specificity was validated by treating with 200 U/mL DNase I (ThermoFisher) for 30 min at 37ºC. Coverslips were blocked in 3% (w/v) BSA, 0.3 M glycine in PBS. Coverslips were then processed as described above, however Triton X-100 was omitted from subsequent buffers to limit permeabilization of the nuclear membrane.

Microscopy and Image Analysis

Fluorescence microscopy was performed using a Zeiss Axio Imager M2 or Zeiss Axio Imager Z2 epifluorescent microscope using a 20x objective. Laser scanning confocal microscopy was performed using a Nikon Eclipse Ti microscope with 40x or 60x oil-immersion objectives.

Images were processed and analysed using FIJI (ImageJ; National Institutes of Health) or CellProfiler (Broad Institute). To analyse nuclear translocation of IRF3, the nuclei and cytoplasm were segmented in CellProfiler using DAPI and vinculin staining, respectively. Mean fluorescence intensity was determined in each compartment and expressed as a ratio of nuclear:cytoplasmic (N:C) intensity. Cells with nuclear translocation were determined as the percentage of cells with an N:C ratio > 1.5.

Quantification of micronuclei (MN)

Cells were grown on glass coverslips, fixed and DAPI-stained as above. Blinded MN scoring was performed using the ImageJ Cell Counter plugin in accordance with published criteria[82]. Mitotic and apoptotic cells were manually excluded from analysis. For detection of cGAS-positive MN, an intensity threshold was set, and cGAS-positive MN were identified by particle analysis in ImageJ. The number of cGAS-positive MN was normalised to the number of cells scored (> 100 cells per independent experiment).

Quantification of cytoplasmic dsDNA

Cytoplasmic dsDNA intensity was analysed on maximum intensity projections of confocal Z-stacks using CellProfiler. Nuclei were segmented based on DAPI staining. The resulting nuclei and TOM20 staining were then used to define the whole-cell boundary and the nuclear region was subtracted from the whole-cell region to define the cytoplasm. Mean fluorescence intensity of the dsDNA signal was then measured in the cytoplasmic compartment. To determine the percentage of cytoplasmic dsDNA-positive cells, dsDNA speckles were enhanced to enable identification as primary objects. The resulting objects were filtered based on mean fluorescence intensity and to improve specificity, cells with at least 10 dsDNA foci were classified as positive for cytoplasmic dsDNA. Identification of the nucleus and consequently the whole cell boundary was reliant on DAPI intensity. As DNase I treatment abolished the DAPI signal, quantification of cytoplasmic intensity could not be performed for DNase I-treated conditions. Five fields of view were analysed per condition.

Wound healing assay

601

602 WT and *STING1* KO HMC3 cells were pre-treated with 10 nM AZD1390 or DMSO as a control

603 for 72 h, then seeded at a density of 79,000 cells/cm^2 into 2-well culture inserts (Ibidi). After

604 24 h, inserts were removed leaving a 500 μm gap, cells were washed twice in PBS then placed

605 in DMEM supplemented with 0.5% HI-FBS to limit proliferation. Wounds were imaged every

606 4 h over a period of 24 h on a Lumascope LS720 (Etaluma Inc) using a 4x phase-contrast

607 objective. Wound closure was analysed in ImageJ and wound area is presented as a

608 percentage of the 0-h time point.

xCELLigence chemotaxis assay

609

610 For preparation of conditioned medium, WT and *STING1* KO HMC3 cells were pre-treated

611 with 10 nM AZD1390 or DMSO as a control for 72 h, then seeded at a density of 21,000

612 cells/cm^2 in 6-well plates. After 48 h, cells were washed in PBS and placed in DMEM

613 supplemented with 0.5% (v/v) HI-FBS. Conditioned medium was centrifuged at 400 *g* for

614 10 min to remove whole cells and debris.

615 Chemotaxis assays were performed using Real-Time Cell Analysis (RTCA) CIM-16 plates

616 (Agilent). The lower chamber contained conditioned medium as the chemoattractant or DMEM

617 supplemented with 0.5% (v/v) HI-FBS as a negative control. The upper chamber was filled

618 with 0.5% (v/v) HI-FBS and plates were left to equilibrate at 37ºC for 1 h. Background

619 impedance (Cell Index) was measured followed by seeding 25,000 cells per well in the upper

620 chamber in technical triplicates. Cells were left to settle at RT for 30 min, then impedance was

621 measured every 15 min for 6 h using an xCELLigence RTCA DP instrument (Agilent). Due to

622 the nature of the assay, absolute cell index values differed between independent experiments

623 precluding presentation of the summarised data.

Statistical Analysis

624

625 Statistical analysis was performed using GraphPad Prism version 9.4.1. Quantitative data is

626 presented as mean ± standard deviation (SD) from at least 3 independent experiments unless

627 stated otherwise. Normality was assessed using Q-Q plots and the Shapiro-Wilk normality

628 test. Student's or Welch's t-tests were used to compare means of two groups with equal or

629 unequal variance, respectively. For comparison of 3 or more groups, one- or two-way ANOVAs

630 were used. P-values ≤ 0.05 were deemed to be statistically significant.

Acknowledgements

Funding

Author contributions

E.J.T. and S.V.K. conceived the study and wrote the manuscript with contributions from L.J. and K.T. E.J.T. performed most of the experiments with the following exceptions. L.J. performed experiments with DNA damaging agents, tissue samples and chemotaxis assays. S.V.K. helped with cell line generation and cell synchronisation experiments. P.T. did the work with iCell microglia and advised on the use of the MSD secretion assay platform. M.D. performed RNA sequencing. K.T. performed bioinformatic analyses of RNA sequencing data. M.P. provided access to the MSD platform. All authors contributed to the data discussion. S.V.K. supervised the work.

Conflicts of interest

The authors declare no conflict of interest.

660 **REFERENCES**

661 1. Lin, X., Kapoor, A., Gu, Y., Chow, M.J., Peng, J., Zhao, K., and Tang, D. (2020).
662   Contributions of DNA Damage to Alzheimer's disease. Int. J. Mol. Sci. *21*, 1666.
663   10.3390/ijms21051666.

664 2. Sun, Y., Curle, A.J., Haider, A.M., and Balmus, G. (2020). The role of DNA damage
665   response in amyotrophic lateral sclerosis. Essays Biochem. *64*, 847–861.
666   10.1042/EBC20200002.

667 3. López-Otín, C., Blasco, M.A., Partridge, L., Serrano, M., and Kroemer, G. (2023).
668   Hallmarks of aging: An expanding universe. Cell *186*, 243–278.
669   10.1016/j.cell.2022.11.001.

670 4. Welch, G., and Tsai, L.-H. (2022). Mechanisms of DNA damage-mediated neurotoxicity in
671   neurodegenerative disease. EMBO Rep. *23*, e54217. 10.15252/embr.202154217.

672 5. Aditi, and McKinnon, P.J. (2022). Genome integrity and inflammation in the nervous
673   system. DNA Repair *119*, 103406. 10.1016/j.dnarep.2022.103406.

674 6. Härtlova, A., Erttmann, S.F., Raffi, F.A.M., Schmalz, A.M., Resch, U., Anugula, S.,
675   Lienenklaus, S., Nilsson, L.M., Kröger, A., Nilsson, J.A., et al. (2015). DNA damage primes
676   the type I interferon system via the cytosolic DNA sensor STING to promote anti-microbial
677   innate immunity. Immunity *42*, 332–343. 10.1016/j.immuni.2015.01.012.

678 7. Decout, A., Katz, J.D., Venkatraman, S., and Ablasser, A. (2021). The cGAS–STING
679   pathway as a therapeutic target in inflammatory diseases. Nat. Rev. Immunol. *21*, 548–
680   569. 10.1038/s41577-021-00524-z.

681 8. Hopfner, K.-P., and Hornung, V. (2020). Molecular mechanisms and cellular functions of
682   cGAS–STING signalling. Nat. Rev. Mol. Cell Biol. *21*, 501–521. 10.1038/s41580-020-
683   0244-x.

684 9. Harding, S.M., Benci, J.L., Irianto, J., Discher, D.E., Minn, A.J., and Greenberg, R.A.
685   (2017). Mitotic progression following DNA damage enables pattern recognition within
686   micronuclei. Nature *548*, 466–470.

687 10. Mackenzie, K.J., Carroll, P., Martin, C.-A., Murina, O., Fluteau, A., Simpson, D.J., Olova,
688   N., Sutcliffe, H., Rainger, J.K., Leitch, A., et al. (2017). cGAS surveillance of micronuclei
689   links genome instability to innate immunity. Nature *548*, 461–465.

690 11. MacDonald, K.M., Nicholson-Puthenveedu, S., Tageldein, M.M., Khasnis, S., Arrowsmith,
691   C.H., and Harding, S.M. (2023). Antecedent chromatin organization determines cGAS
692   recruitment to ruptured micronuclei. Nat. Commun. *14*, 556. 10.1038/s41467-023-36195-
693   8.

694 12. Song, X., Aw, J.T.M., Ma, F., Cheung, M.F., Leung, D., and Herrup, K. (2021). DNA repair
695   inhibition leads to active export of repetitive sequences to the cytoplasm triggering an
696   inflammatory response. J. Neurosci. *41*, 9286–9307. 10.1523/JNEUROSCI.0845-
697   21.2021.

698 13. West, A.P., Khoury-Hanold, W., Staron, M., Tal, M.C., Pineda, C.M., Lang, S.M., Bestwick,
699   M., Duguay, B.A., Raimundo, N., MacDuff, D.A., et al. (2015). Mitochondrial DNA stress

primes the antiviral innate immune response. Nature *520*, 553–557. 10.1038/nature14156.

14. Crossley, M.P., Song, C., Bocek, M.J., Choi, J.-H., Kousorous, J., Sathirachinda, A., Lin, C., Brickner, J.R., Bai, G., Lans, H., et al. (2023). R-loop-derived cytoplasmic RNA–DNA hybrids activate an immune response. Nature *613*, 187–194. 10.1038/s41586-022-05545-9.

15. Chen, Y.-A., Shen, Y.-L., Hsia, H.-Y., Tiang, Y.-P., Sung, T.-L., and Chen, L.-Y. (2017). Extrachromosomal telomere repeat DNA is linked to ALT development via cGAS-STING DNA sensing pathway. Nat. Struct. Mol. Biol. *24*, 1124–1131. 10.1038/nsmb.3498.

16. Reinert, L.S., Lopušná, K., Winther, H., Sun, C., Thomsen, M.K., Nandakumar, R., Mogensen, T.H., Meyer, M., Vægter, C., Nyengaard, J.R., et al. (2016). Sensing of HSV-1 by the cGAS–STING pathway in microglia orchestrates antiviral defence in the CNS. Nat. Commun. *7*, 13348.

17. Paolicelli, R.C., Bolasco, G., Pagani, F., Maggi, L., Scianni, M., Panzanelli, P., Giustetto, M., Ferreira, T.A., Guiducci, E., Dumas, L., et al. (2011). Synaptic pruning by microglia is necessary for normal brain development. Science *333*, 1456–1458. 10.1126/science.1202529.

18. Schafer, D.P., Lehrman, E.K., Kautzman, A.G., Koyama, R., Mardinly, A.R., Yamasaki, R., Ransohoff, R.M., Greenberg, M.E., Barres, B.A., and Stevens, B. (2012). Microglia sculpt postnatal neural circuits in an activity and complement-dependent manner. Neuron *74*, 691–705. 10.1016/j.neuron.2012.03.026.

19. Bellver-Landete, V., Bretheau, F., Mailhot, B., Vallières, N., Lessard, M., Janelle, M.-E., Vernoux, N., Tremblay, M.-È., Fuehrmann, T., Shoichet, M.S., et al. (2019). Microglia are an essential component of the neuroprotective scar that forms after spinal cord injury. Nat. Commun. *10*, 518. 10.1038/s41467-019-08446-0.

20. Sierra, A., Encinas, J.M., Deudero, J.J.P., Chancey, J.H., Enikolopov, G., Overstreet-Wadiche, L.S., Tsirka, S.E., and Maletic-Savatic, M. (2010). Microglia shape adult hippocampal neurogenesis through apoptosis-coupled phagocytosis. Cell Stem Cell *7*, 483–495. 10.1016/j.stem.2010.08.014.

21. Muzio, L., Viotti, A., and Martino, G. (2021). Microglia in neuroinflammation and neurodegeneration: from understanding to therapy. Front. Neurosci. *15*, 742065.

22. Hickman, S., Izzy, S., Sen, P., Morsett, L., and Khoury, J.E. (2018). Microglia in neurodegeneration. Nat. Neurosci. *21*, 1359–1369. 10.1038/s41593-018-0242-x.

23. Shiloh, Y., and Lederman, H.M. (2017). Ataxia-telangiectasia (A-T): an emerging dimension of premature ageing. Ageing Res. Rev. *33*, 76–88. 10.1016/j.arr.2016.05.002.

24. Bourseguin, J., Cheng, W., Talbot, E., Hardy, L., Lai, J., Jeffries, A.M., Lodato, M.A., Lee, E.A., and Khoronenkova, S.V. (2022). Persistent DNA damage associated with ATM kinase deficiency promotes microglial dysfunction. Nucleic Acids Res. *50*, 2700–2718. 10.1093/nar/gkac104.

25. Quek, H., Luff, J., Cheung, K.G., Kozlov, S., Gatei, M., Lee, C.S., Bellingham, M.C., Noakes, P.G., Lim, Y.C., Barnett, N.L., et al. (2017). A rat model of ataxia-telangiectasia: evidence for a neurodegenerative phenotype. Hum. Mol. Genet. *26*, 109–123. 10.1093/hmg/ddw371.

26. Song, X., Ma, F., and Herrup, K. (2019). Accumulation of cytoplasmic DNA due to ATM deficiency activates the microglial viral response system with neurotoxic consequences. J. Neurosci. *39*, 6378–6394. 10.1523/JNEUROSCI.0774-19.2019.

27. Levi, H., Bar, E., Cohen-Adiv, S., Sweitat, S., Kanner, S., Galron, R., Mitiagin, Y., and Barzilai, A. (2022). Dysfunction of cerebellar microglia in ataxia-telangiectasia. Glia *70*, 536–557. 10.1002/glia.24122.

28. Quek, H., Luff, J., Cheung, K., Kozlov, S., Gatei, M., Lee, C.S., Bellingham, M.C., Noakes, P.G., Lim, Y.C., Barnett, N.L., et al. (2016). Rats with a missense mutation in Atm display neuroinflammation and neurodegeneration subsequent to accumulation of cytosolic DNA following unrepaired DNA damage. J. Leukoc. Biol. *101*, 927–947. 10.1189/jlb.4vma0716-316r.

29. Grabert, K., Michoel, T., Karavolos, M.H., Clohisey, S., Baillie, J.K., Stevens, M.P., Freeman, T.C., Summers, K.M., and McColl, B.W. (2016). Microglial brain region−dependent diversity and selective regional sensitivities to aging. Nat. Neurosci. *19*, 504–516. 10.1038/nn.4222.

30. Tay, T.L., Mai, D., Dautzenberg, J., Fernández-Klett, F., Lin, G., Sagar, Datta, M., Drougard, A., Stempfl, T., Ardura-Fabregat, A., et al. (2017). A new fate mapping system reveals context-dependent random or clonal expansion of microglia. Nat. Neurosci. *20*, 793–803. 10.1038/nn.4547.

31. Lai, J., Kim, J., Jeffries, A.M., Tolles, A., Chittenden, T.W., Buckley, P.G., Yu, T.W., Lodato, M.A., and Lee, E.A. (2021). Single-nucleus transcriptomic analyses reveal microglial activation underlying cerebellar degeneration in Ataxia Telangiectasia.

32. Aguado, J., Chaggar, H.K., Gómez-Inclán, C., Shaker, M.R., Leeson, H.C., Mackay-Sim, A., and Wolvetang, E.J. (2021). Inhibition of the cGAS-STING pathway ameliorates the premature senescence hallmarks of Ataxia-Telangiectasia brain organoids. Aging Cell *20*, e13468. 10.1111/acel.13468.

33. Hu, M., Zhou, M., Bao, X., Pan, D., Jiao, M., Liu, X., Li, F., and Li, C.-Y. (2021). ATM inhibition enhances cancer immunotherapy by promoting mtDNA leakage and cGAS/STING activation. J. Clin. Invest. *131*, e139333. 10.1172/JCI139333.

34. Zhang, Q., Green, M.D., Lang, X., Lazarus, J., Parsels, J.D., Wei, S., Parsels, L.A., Shi, J., Ramnath, N., Wahl, D.R., et al. (2019). Inhibition of ATM increases interferon signaling and sensitizes pancreatic cancer to immune checkpoint blockade therapy. Cancer Res. *79*, 3940–3951. 10.1158/0008-5472.CAN-19-0761.

35. Yang, B., Dan, X., Hou, Y., Lee, J.-H., Wechter, N., Krishnamurthy, S., Kimura, R., Babbar, M., Demarest, T., McDevitt, R., et al. (2021). NAD+ supplementation prevents STING-induced senescence in ataxia telangiectasia by improving mitophagy. Aging Cell *20*, e13329. 10.1111/acel.13329.

36. Concannon, P., and Gatti, R.A. (1997). Diversity of ATM gene mutations detected in patients with ataxia-telangiectasia. Hum. Mutat. *10*, 100–107. 10.1002/(SICI)1098-1004(1997)10:2<100::AID-HUMU2>3.0.CO;2-O.

37. Sakasai, R., Teraoka, H., Takagi, M., and Tibbetts, R.S. (2010). Transcription-dependent activation of ataxia telangiectasia mutated prevents DNA-dependent protein kinase-mediated cell death in response to topoisomerase I poison. J. Biol. Chem. *285*, 15201–15208. 10.1074/jbc.M110.101808.

787 38. Ramanjulu, J.M., Pesiridis, G.S., Yang, J., Concha, N., Singhaus, R., Zhang, S.-Y., Tran, J.-L., Moore, P., Lehmann, S., Eberl, H.C., et al. (2018). Design of amidobenzimidazole STING receptor agonists with systemic activity. Nature *564*, 439–443. 10.1038/s41586-018-0705-y.

791 39. Durant, S.T., Zheng, L., Wang, Y., Chen, K., Zhang, L., Zhang, T., Yang, Z., Riches, L., Trinidad, A.G., Fok, J.H.L., et al. (2018). The brain-penetrant clinical ATM inhibitor AZD1390 radiosensitizes and improves survival of preclinical brain tumor models. Sci. Adv. *4*, eaat1719. 10.1126/sciadv.aat1719.

795 40. Trifonova, R.T., and Barteneva, N.S. (2018). Quantitation of IRF3 nuclear translocation in heterogeneous cellular populations from cervical tissue using imaging flow cytometry. In Cellular Heterogeneity: Methods and Protocols Methods in Molecular Biology., N. S. Barteneva and I. A. Vorobjev, eds. (Springer), pp. 125–153.

799 41. Gómez-Nicola, D., Fransen, N.L., Suzzi, S., and Perry, V.H. (2013). Regulation of microglial proliferation during chronic neurodegeneration. J. Neurosci. *33*, 2481–2493. 10.1523/JNEUROSCI.4440-12.2013.

802 42. Huang, Y., Xu, Z., Xiong, S., Sun, F., Qin, G., Hu, G., Wang, J., Zhao, L., Liang, Y.-X., Wu, T., et al. (2018). Repopulated microglia are solely derived from the proliferation of residual microglia after acute depletion. Nat. Neurosci. *21*, 530–540. 10.1038/s41593-018-0090-8.

806 43. Yamamoto, K., Wang, J., Sprinzen, L., Xu, J., Haddock, C.J., Li, C., Lee, B.J., Loredan, D.G., Jiang, W., Vindigni, A., et al. (2016). Kinase-dead ATM protein is highly oncogenic and can be preferentially targeted by Topo-isomerase I inhibitors. eLife *5*, e14709. 10.7554/eLife.14709.

810 44. Yamamoto, K., Wang, Y., Jiang, W., Liu, X., Dubois, R.L., Lin, C.-S., Ludwig, T., Bakkenist, C.J., and Zha, S. (2012). Kinase-dead ATM protein causes genomic instability and early embryonic lethality in mice. J. Cell Biol. *198*, 305–313. 10.1083/jcb.201204098.

813 45. Kranzusch, P.J., Lee, A.S.-Y., Berger, J.M., and Doudna, J.A. (2013). Structure of Human cGAS Reveals a Conserved Family of Second-Messenger Enzymes in Innate Immunity. Cell Rep. *3*, 1362–1368. 10.1016/j.celrep.2013.05.008.

816 46. Valentin-Vega, Y.A., MacLean, K.H., Tait-Mulder, J., Milasta, S., Steeves, M., Dorsey, F.C., Cleveland, J.L., Green, D.R., and Kastan, M.B. (2012). Mitochondrial dysfunction in ataxia-telangiectasia. Blood *119*, 1490–1500. 10.1182/blood-2011-08-373639.

819 47. Pillai, S., Nguyen, J., Johnson, J., Haura, E., Coppola, D., and Chellappan, S. (2015). Tank binding kinase 1 is a centrosome-associated kinase necessary for microtubule dynamics and mitosis. Nat. Commun. *6*, 10072. 10.1038/ncomms10072.

822 48. Sarraf, S.A., Sideris, D.P., Giagtzoglou, N., Ni, L., Kankel, M.W., Sen, A., Bochicchio, L.E., Huang, C.-H., Nussenzweig, S.C., Worley, S.H., et al. (2019). PINK1/Parkin influences cell cycle by sequestering TBK1 at damaged mitochondria, inhibiting mitosis. Cell Rep. *29*, 225-235.e5. 10.1016/j.celrep.2019.08.085.

826 49. Dunphy, G., Flannery, S.M., Almine, J.F., Connolly, D.J., Paulus, C., Jønsson, K.L., Jakobsen, M.R., Nevels, M.M., Bowie, A.G., and Unterholzner, L. (2018). Non-canonical activation of the DNA sensing adaptor STING by ATM and IFI16 mediates NF-κB signaling after nuclear DNA damage. Mol. Cell *71*, 745-760.e5. 10.1016/j.molcel.2018.07.034.

830 50. Chu, T.-T., Tu, X., Yang, K., Wu, J., Repa, J.J., and Yan, N. (2021). Tonic prime-boost of
831   STING signalling mediates Niemann–Pick disease type C. Nature *596*, 570–575.
832   10.1038/s41586-021-03762-2.

833 51. de Oliveira Mann, C.C., Orzalli, M.H., King, D.S., Kagan, J.C., Lee, A.S.Y., and Kranzusch,
834   P.J. (2019). Modular architecture of the STING C-terminal tail allows interferon and NF-
835   κB signaling adaptation. Cell Rep. *27*, 1165-1175.e5.
836   https://doi.org/10.1016/j.celrep.2019.03.098.

837 52. Hughes, C.E., and Nibbs, R.J.B. (2018). A guide to chemokines and their receptors. Febs
838   J. *285*, 2944–2971. 10.1111/febs.14466.

839 53. Holm, C.K., Jensen, S.B., Jakobsen, M.R., Cheshenko, N., Horan, K.A., Moeller, H.B.,
840   Gonzalez-Dosal, R., Rasmussen, S.B., Christensen, M.H., Yarovinsky, T.O., et al. (2012).
841   Virus-cell fusion as a trigger of innate immunity dependent on the adaptor STING. Nat.
842   Immunol. *13*, 737–743. 10.1038/ni.2350.

843 54. Marques, J.T., and Williams, B.R.G. (2005). Activation of the mammalian immune system
844   by siRNAs. Nat. Biotechnol. *23*, 1399–1405. 10.1038/nbt1161.

845 55. Nimmerjahn, A., Kirchhoff, F., and Helmchen, F. (2005). Resting microglial cells are highly
846   dynamic surveillants of brain parenchyma in vivo. Science *308*, 1314–1318.
847   10.1126/science.1110647.

848 56. Limame, R., Wouters, A., Pauwels, B., Fransen, E., Peeters, M., Lardon, F., Wever, O.D.,
849   and Pauwels, P. (2012). Comparative Analysis of Dynamic Cell Viability, Migration and
850   Invasion Assessments by Novel Real-Time Technology and Classic Endpoint Assays.
851   PLOS ONE *7*, e46536. 10.1371/journal.pone.0046536.

852 57. Balmus, G., Pilger, D., Coates, J., Demir, M., Sczaniecka-Clift, M., Barros, A.C., Woods,
853   M., Fu, B., Yang, F., Chen, E., et al. (2019). ATM orchestrates the DNA-damage response
854   to counter toxic non-homologous end-joining at broken replication forks. Nat. Commun.
855   *10*, 87. 10.1038/s41467-018-07729-2.

856 58. Wilson, D.M., Cookson, M.R., Van Den Bosch, L., Zetterberg, H., Holtzman, D.M., and
857   Dewachter, I. (2023). Hallmarks of neurodegenerative diseases. Cell *186*, 693–714.
858   10.1016/j.cell.2022.12.032.

859 59. Aw, E., Zhang, Y., and Carroll, M. (2020). Microglial responses to peripheral type 1
860   interferon. J. Neuroinflammation *17*, 340. 10.1186/s12974-020-02003-z.

861 60. Li, W., Viengkhou, B., Denyer, G., West, P.K., Campbell, I.L., and Hofer, M.J. (2018).
862   Microglia have a more extensive and divergent response to interferon- a compared with
863   astrocytes. Glia *66*, 2058–2078. 10.1002/glia.23460.

864 61. Rappert, A. (2004). CXCR3-Dependent Microglial Recruitment Is Essential for Dendrite
865   Loss after Brain Lesion. J. Neurosci. *24*, 8500–8509. 10.1523/JNEUROSCI.2451-
866   04.2004.

867 62. Festa, B.P., Siddiqi, F.H., Jimenez-Sanchez, M., Won, H., Rob, M., Djajadikerta, A.,
868   Stamatakou, E., and Rubinsztein, D.C. (2023). Microglial-to-neuronal CCR5 signaling
869   regulates autophagy in neurodegeneration. Neuron *0*. 10.1016/j.neuron.2023.04.006.

870 63. Haruwaka, K., Ikegami, A., Tachibana, Y., Ohno, N., Konishi, H., Hashimoto, A.,
871   Matsumoto, M., Kato, D., Ono, R., Kiyama, H., et al. (2019). Dual microglia effects on

872   blood brain barrier permeability induced by systemic inflammation. Nat. Commun. *10*,
873   5816. 10.1038/s41467-019-13812-z.

874   64. Chen, X., Firulyova, M., Manis, M., Herz, J., Smirnov, I., Aladyeva, E., Wang, C., Bao, X.,
875   Finn, M.B., Hu, H., et al. (2023). Microglia-mediated T cell infiltration drives
876   neurodegeneration in tauopathy. Nature *615*, 668–677. 10.1038/s41586-023-05788-0.

877   65. Anastasiou, M., Newton, G.A., Kaur, K., Carrillo-Salinas, F.J., Smolgovsky, S.A., Bayer,
878   A.L., Ilyukha, V., Sharma, S., Poltorak, A., Luscinskas, F.W., et al. (2021). Endothelial
879   STING controls T cell transmigration in an IFNI-dependent manner. JCI Insight *6*,
880   e149346. 10.1172/jci.insight.149346.

881   66. Nagata, M., Kosaka, A., Yajima, Y., Yasuda, S., Ohara, M., Ohara, K., Harabuchi, S.,
882   Hayashi, R., Funakoshi, H., Ueda, J., et al. (2021). A critical role of STING-triggered tumor-
883   migrating neutrophils for anti-tumor effect of intratumoral cGAMP treatment. Cancer
884   Immunol. Immunother. *70*, 2301–2312. 10.1007/s00262-021-02864-0.

885   67. Tan, J., Ge, Y., Zhang, M., and Ding, M. (2023). Proteomics analysis uncovers
886   plasminogen activator PLAU as a target of the STING pathway for suppression of cancer
887   cell migration and invasion. J. Biol. Chem. *299*. 10.1016/j.jbc.2022.102779.

888   68. Tolbert, C.E., Beck, M.V., Kilmer, C.E., and Srougi, M.C. (2019). Loss of ATM positively
889   regulates Rac1 activity and cellular migration through oxidative stress. Biochem. Biophys.
890   Res. Commun. *508*, 1155–1161. 10.1016/j.bbrc.2018.12.033.

891   69. Stowell, R.D., Wong, E.L., Batchelor, H.N., Mendes, M.S., Lamantia, C.E., Whitelaw, B.S.,
892   and Majewska, A.K. (2018). Cerebellar microglia are dynamically unique and survey
893   Purkinje   neurons   in   vivo.   Dev.   Neurobiol.   *78*,   627–644.
894   https://doi.org/10.1002/dneu.22572.

895   70. Gulen, M.F., Samson, N., Keller, A., Schwabenland, M., Liu, C., Glück, S., Thacker, V.V.,
896   Favre, L., Mangeat, B., Kroese, L.J., et al. (2023). cGAS–STING drives ageing-related
897   inflammation and neurodegeneration. Nature, 1–7. 10.1038/s41586-023-06373-1.

898   71. Janabi, N., Peudenier, S., Héron, B., Ng, K.H., and Tardieu, M. (1995). Establishment of
899   human microglial cell lines after transfection of primary cultures of embryonic microglial
900   cells with the SV40 large T antigen. Neurosci. Lett. *195*, 105–108. 10.1016/0304-
901   3940(94)11792-H.

902   72. Garcia-Mesa, Y., Jay, T.R., Checkley, M.A., Luttge, B., Dobrowolski, C., Valadkhan, S.,
903   Landreth, G.E., Karn, J., and Alvarez-Carbonell, D. (2017). Immortalization of primary
904   microglia: a new platform to study HIV regulation in the central nervous system. J.
905   Neurovirol. *23*, 47–66. 10.1007/s13365-016-0499-3.

906   73. Ran, F.A., Hsu, P.D., Wright, J., Agarwala, V., Scott, D.A., and Zhang, F. (2013). Genome
907   engineering   using   the   CRISPR-Cas9   system.   Nat.   Protoc.   *8*,   2281–2308.
908   10.1038/nprot.2013.143.

909   74. Botling, J., and Micke, P. (2011). Fresh frozen tissue: RNA extraction and quality control.
910   In Methods in Biobanking Methods in Molecular Biology., J. Dillner, ed. (Humana Press),
911   pp. 405–413.

912   75. Livak, K.J., and Schmittgen, T.D. (2001). Analysis of relative gene expression data using
913   real-time quantitative PCR and the 2-$\Delta\Delta$CT method. Methods *25*, 402–408.
914   10.1006/meth.2001.1262.

915   76. Krueger, F., James, F., Ewels, P., Afyounian, E., and Schuster-Boeckler, B. (2021).
916   TrimGalore: v0.6.7. 10.5281/zenodo.5127899.

917   77. Andrews, S. (2020). FastQC: v0.11.9.
918   https://www.bioinformatics.babraham.ac.uk/projects/fastqc/.

919   78. Shannon, P., Markiel, A., Ozier, O., Baliga, N.S., Wang, J.T., Ramage, D., Amin, N.,
920   Schwikowski, B., and Ideker, T. (2003). Cytoscape: a software environment for integrated
921   models of biomolecular interaction networks. Genome Res. *13*, 2498–2504.
922   10.1101/gr.1239303.

923   79. Doncheva, N.T., Morris, J.H., Gorodkin, J., and Jensen, L.J. (2019). Cytoscape StringApp:
924   Network Analysis and Visualization of Proteomics Data. J. Proteome Res. *18*, 623–632.
925   10.1021/acs.jproteome.8b00702.

926   80. Wu, T., Hu, E., Xu, S., Chen, M., Guo, P., Dai, Z., Feng, T., Zhou, L., Tang, W., Zhan, L.,
927   et al. (2021). clusterProfiler 4.0: A universal enrichment tool for interpreting omics data.
928   The Innovation *2*, 100141. 10.1016/j.xinn.2021.100141.

929   81. Lam, A.R., Bert, N.L., Ho, S.S.W., Shen, Y.J., Tang, M.L.F., Xiong, G.M., Croxford, J.L.,
930   Koo, C.X., Ishii, K.J., Akira, S., et al. (2014). RAE1 ligands for the NKG2D receptor are
931   regulated by STING-dependent DNA sensor pathways in lymphoma. Cancer Res. *74*,
932   2193–2203. 10.1158/0008-5472.CAN-13-1703.

933   82. Fenech, M., Chang, W.P., Kirsch-Volders, M., Holland, N., Bonassi, S., and Zeiger, E.
934   (2003). HUMN project: Detailed description of the scoring criteria for the cytokinesis-block
935   micronucleus assay using isolated human lymphocyte cultures. Mutat. Res. - Genet.
936   Toxicol. Environ. Mutagen. *534*, 65–75. 10.1016/S1383-5718(02)00249-8.

937   83. Talbot, E. (2023). Mechanisms of cytosolic DNA sensing and neuroinflammation in ataxia-
938   telangiectasia. [Apollo - University of Cambridge Repository].
939   https://doi.org/10.17863/CAM.97149.

FIGURE LEGENDS

Figure 1: Loss of ATM function in human microglia-derived cells drives STING pathway activation and a type I interferon response.

(A) Representative immunoblot of STING pathway activation in *ATM* KO C20 cells (clones #1 and #2). Loading control: Vinculin. Quantification of phosphorylated proteins is relative to respective total proteins and normalised to WT.

(B) Relative mRNA levels of *IFNB1* and *IFIT2* in WT and *ATM* KO C20 cells treated with 1 µM STING agonist diABZI, or DMSO as control, for 5 h. C_q values normalised to *IPO8* and DMSO-treated WT cells. Mean $\log_2$ fold change ± SD (n=3). Two-way ANOVA with Tukey's post-hoc comparison test.

(C) Representative immunoblot of HMC3 cells treated with 10 nM ATM inhibitor AZD1390 (ATMi), or DMSO as control, for 1, 3, 6 or 9 days. Loading control: Vinculin. NS: nonspecific. Quantification of phosphorylated proteins is relative to respective total proteins and normalised to Day 1 DMSO control.

(D) Representative images of IRF3 localisation in HMC3 cells stimulated for 2 h with 1 µM diABZI, or DMSO as control, or with 10 nM ATMi or DMSO for 6 days (diABZI and ATMi stimulation are part of separate experiments). Red: IRF3, cyan: DNA (DAPI). 20x magnification, scale bar = 25 µm. Yellow arrows indicate cells with nuclear IRF3.

(E) Percentage of cells with nuclear translocation of IRF3 treated as in (D). Mean ± SD (n=3). Unpaired, two-tailed Student's *t*-tests.

(F) Relative *IFNB1* mRNA levels in HMC3 cells treated with ATMi or DMSO for 6 days followed by 1 µM diABZI, or DMSO as a control, for 5 h. C_q values normalised to *RPS13* and DMSO-treated cells. Mean $\log_2$ fold change ± SD (n=3). Two-way ANOVA with Tukey's post-hoc comparison test.

*p ≤ 0.05; **p ≤ 0.01; ***p ≤ 0.001; ****p ≤ 0.0001; ns = not significant.

Figure 2: Loss of ATM function leads to cGAS accumulation at micronuclei.

(A) Representative immunoblot of HMC3 cells treated with 10 nM AZD1390 (ATMi), or DMSO as a control, for 6 days followed by 4-day ATMi washout. To confirm ATM inhibition, cells were treated with 1 µM camptothecin (CPT) or DMSO as a control for 1 h. Loading control: GAPDH. Quantification of ATM^{pS1981} and CHK2^{pT68} is relative to respective total proteins.

(B) Representative images of micronuclei (MN) in HMC3 cells treated as in (A). Yellow arrows indicate MN visualised by DAPI staining. 20x magnification, scale bar = 15 µm.

973 **(C)** Quantification of MN frequency as in (B). Mean ± SD (n=3). Two-way ANOVA with

974 Tukey's post-hoc comparison test.

975 **(D)** Representative images of MN in WT and *ATM* KO C20 cells. Yellow arrows indicate MN

976 visualised by DAPI staining. 20x magnification, scale bar = 15 μm.

977 **(E)** Quantification of MN frequency as in (D). Mean ± SD (n=4). One-way ANOVA with

978 Tukey's post-hoc comparison test.

979 **(F)** Representative images of MN negative (cGAS$^-$ MN) or positive (cGAS$^+$ MN) for cGAS.

980 Yellow arrows indicate MN. Blue: DAPI, green: cGAS. 20x magnification, scale bar = 15 μm.

981 **(G)** Quantification of cGAS$^+$ and cGAS$^-$ MN in HMC3 cells treated with ATMi or DMSO for

982 6 days. MN frequency per cell is shown. Mean ± SD (n=3). Two-way ANOVA with Tukey's

983 post-hoc comparison test.

984 **(H)** Quantification of cGAS$^+$ and cGAS$^-$ MN in WT and *ATM* KO C20 cells. MN frequency per

985 cell is shown. Mean ± SD (n=3). Two-way ANOVA with Tukey's post-hoc comparison test.

986 *$p \leq 0.05$; ****$p \leq 0.0001$; ns = not significant.

987 **Figure 3: STING activation and type I interferon signalling in ATM deficiency are**

988 **dependent on cGAS.**

989 **(A)** Representative immunoblot of siRNA-mediated cGAS and STING depletion in HMC3

990 cells treated with 10 nM ATMi, or DMSO as a control, for 6 days. Positive control: 7 μM

991 2',3'-cGAMP for 1.5 h delivered by digitonin permeabilization, mock: digitonin

992 permeabilization. Loading control: α/β-tubulin. NS: nonspecific.

993 **(B)** Representative immunoblot of IRF3^{pS396} and STAT1^{pY701} levels in cytosolic and nuclear

994 extracts of HMC3 cells as in (A). Cytoplasmic marker: GAPDH; nuclear marker: fibrillarin.

995 **(C)** Relative mRNA levels of *IFNB1*, *IFIT2*, and *IL6* of cells as in (A). C_q values normalised to

996 *RPS13* of cells treated with control (Ctrl) siRNA and DMSO. Mean $\log_2$ fold change ± SD

997 (n=3). Two-way ANOVA with Tukey's post-hoc comparison test.

998 **$p \leq 0.01$; ****$p \leq 0.0001$; ns = not significant.

999 **Figure 4: Migration-related pathways and chemotaxis genes are enriched in**

1000 **iPSC-derived microglia stimulated with IFN-β.**

1001 **(A)** Schematic of experimental workflow. iCell microglia were treated with vehicle or 5 ng/mL

1002 human IFN-β (hIFN-β) for 6 or 24 h (n = 3), followed by bulk RNAseq.

1003 **(B)** Dotplot of top 20 GO biological processes enriched among differentially expressed

1004 genes (DEGs) in IFN-β-treated iCell microglia. Migration-related processes highlighted in

1005   teal.

1006   **(C)** STING network analysis of significantly differentially expressed genes (adjusted p-value

1007   < 0.05) related to cell chemotaxis at 6 and 24 h of IFN-β-treated compared to vehicle-treated

1008   cells. Colour scale represents $\log_2$ fold change (Log2FC).

1009   **(D)** Heatmap shows gene expression changes (Log2FC) of significantly differentially

1010   expressed chemokine family genes in cells treated as in (A). Grey indicates the genes that

1011   are not significantly differentially expressed (adjusted p-value > 0.05).

1012   **Figure 5: Loss of ATM function leads to STING-dependent chemokine secretion.**

1013   **(A)** Relative mRNA levels of *CCL5* and *CXCL10* in WT and *ATM* KO C20 cells and upon

1014   treatment with 1 μM diABZI, or DMSO as control, for 5 h. C_q values normalised to *IPO8* and

1015   DMSO-treated WT cells. Mean $\log_2$ fold change ± SD (n=3). Two-way ANOVA with Tukey's

1016   post-hoc comparison test.

1017   **(B)** Schematic of experimental workflow. WT and *STING1* KO HMC3 cells were treated with

1018   10 nM ATMi, or DMSO as a control, for 6 days. mRNA levels were measured by RT-qPCR.

1019   Secretion was measured 24 h after media change to low FBS supplemented with 1 μM

1020   diABZI, or DMSO as a control.

1021   **(C)** Relative mRNA levels of *CCL5* and *CXCL10* from cells treated as in (B). C_q values

1022   normalised to *RPS13* and DMSO-treated WT cells. Mean $\log_2$ fold change ± SD (n=3).

1023   Two-way ANOVA with Tukey's post-hoc comparison test.

1024   **(D)** CXCL10 concentration in cell culture supernatants. Mean ± SD (n=3). Dashed line

1025   indicates lower limit of detection (LLOD) = 0.12 pg/mL. Nd: not detected. One-way ANOVA

1026   with Tukey's post-hoc comparison test in WT cells.

1027   **(E)** Representative immunoblot of cerebellar homogenates from individuals with A-T and

1028   matched individuals with no known diseases of the CNS as controls (Ctrl). Loading control:

1029   GAPDH. NS = nonspecific.

1030   **(F)** Relative mRNA levels of *STING1*, *CGAS*, *CCL5,* and *CXCL10* as in (E). C_q values

1031   normalised to *RPS13*. Mean $2^{-\delta CT}$ ± SD shown (n=3). Paired *t*-test.

1032   *p ≤ 0.05; **p ≤ 0.01; ***p ≤ 0.001; ****p ≤ 0.0001; ns = not significant.

1033   **Figure 6: STING regulates microglial chemotaxis**
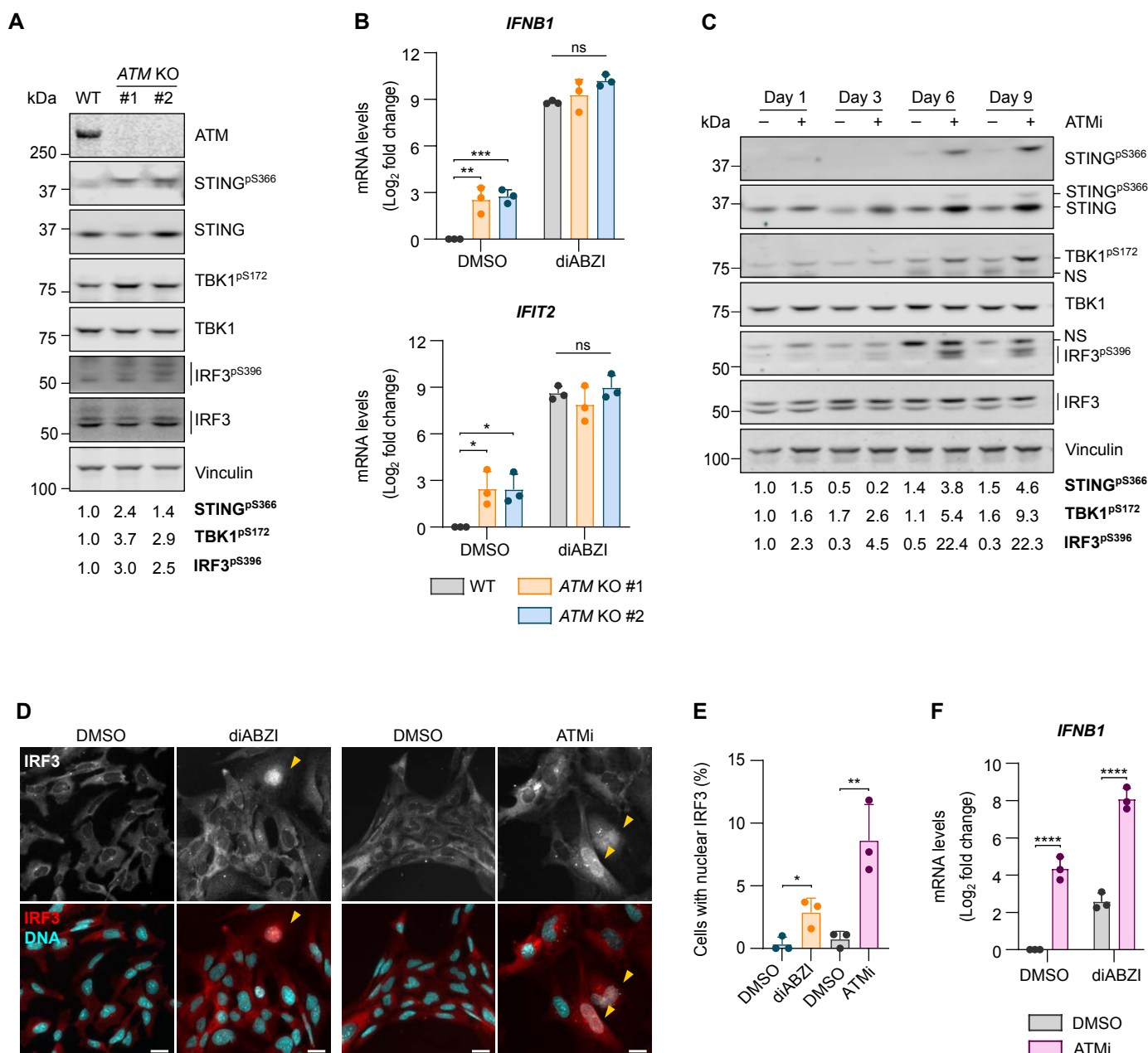
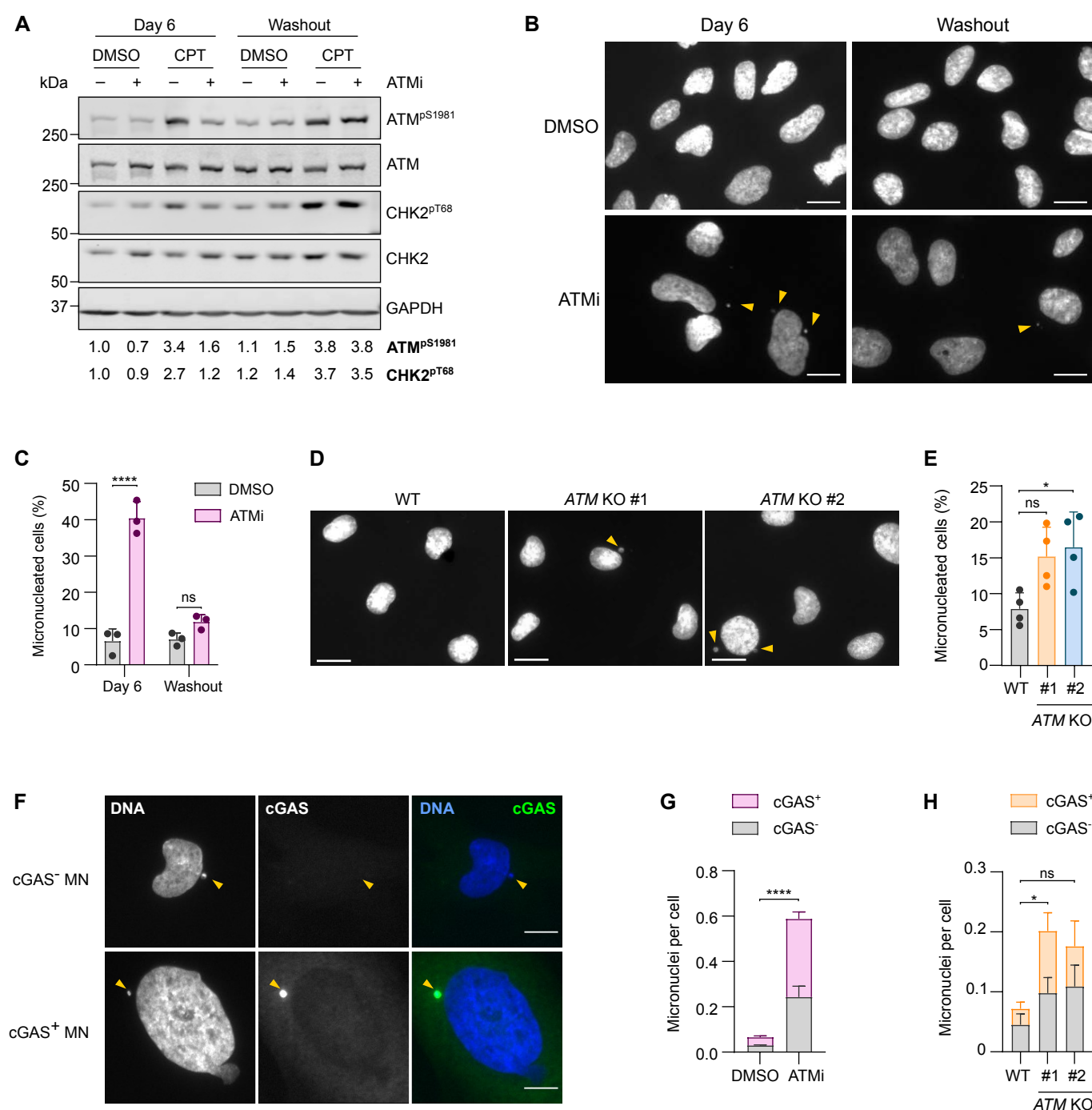1034   **(A)** Schematic of experimental workflow for wound healing migration assay.

1035   **(B)** Representative phase contrast microscopy images of gap area at 0 and 24 h in WT and

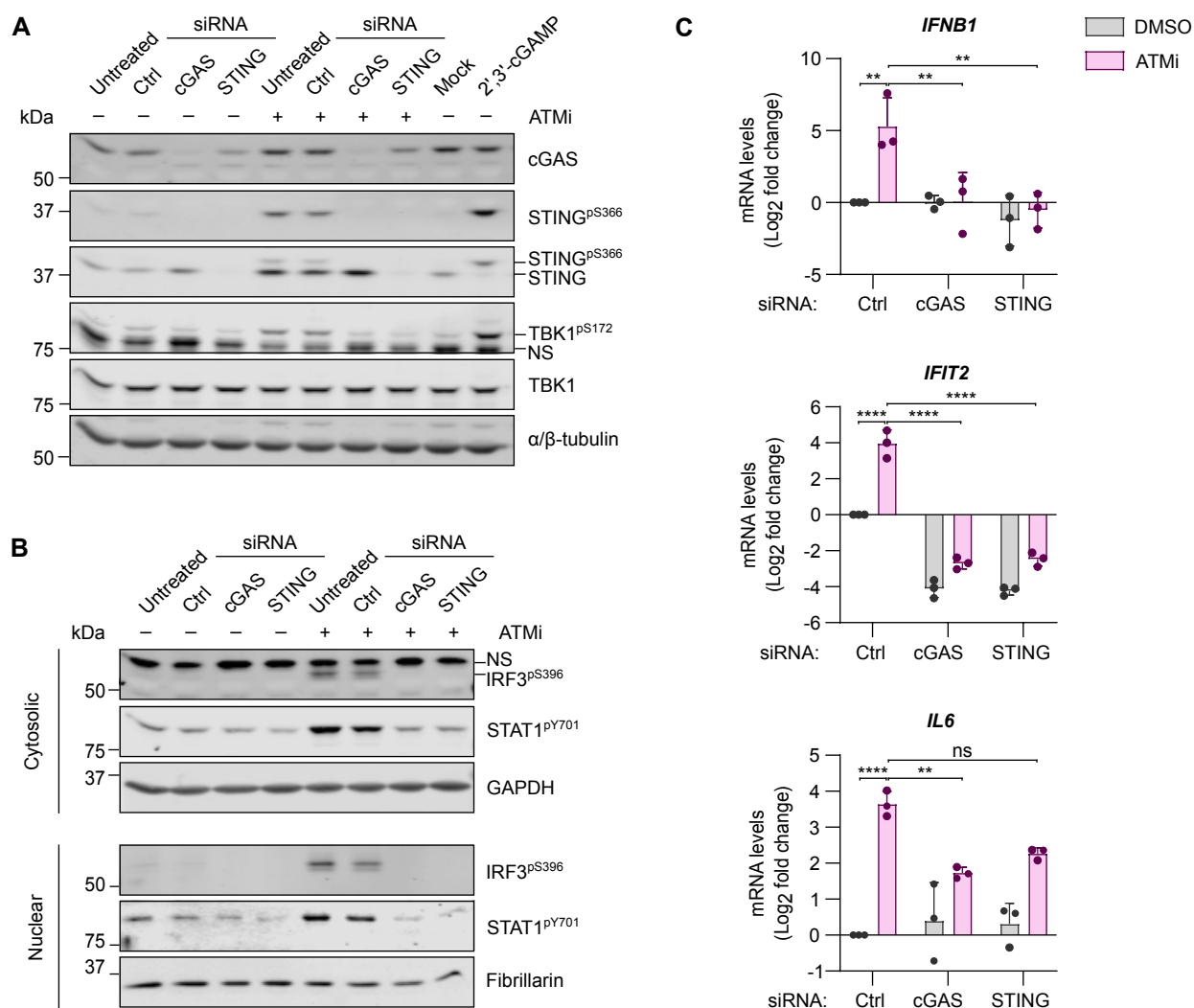1036   *STING1* KO HMC3 cells. 4x magnification, scale bar = 250 μm.

1037   **(C)** Normalised gap area expressed as a percentage of gap area at 0 h. Mean ± SD (n = 3).

1038   Area under curve analysed using one-way ANOVA with Tukey's post-hoc comparison test.

1039   **(D)** Schematic of experimental workflow for xCELLigence chemotaxis assay. WT and

1040   *STING1* KO HMC3 cells were treated with 10 nM ATMi, or DMSO as a control, for 6 days.

1041   Chemotactic migration towards the respective conditioned medium was measured.

1042   **(E)** Kinetics of microglial chemotaxis of cells as in (D). Mean ± SD (n = 3 technical

1043   replicates). Representative of 3 independent experiments. Two-way ANOVA with Tukey's

1044   post-hoc comparison test.

1045   **p ≤ 0.01; ****p ≤ 0.0001.

1046   **Figure 7: Proposed model of STING-dependent regulation of microglial function in**
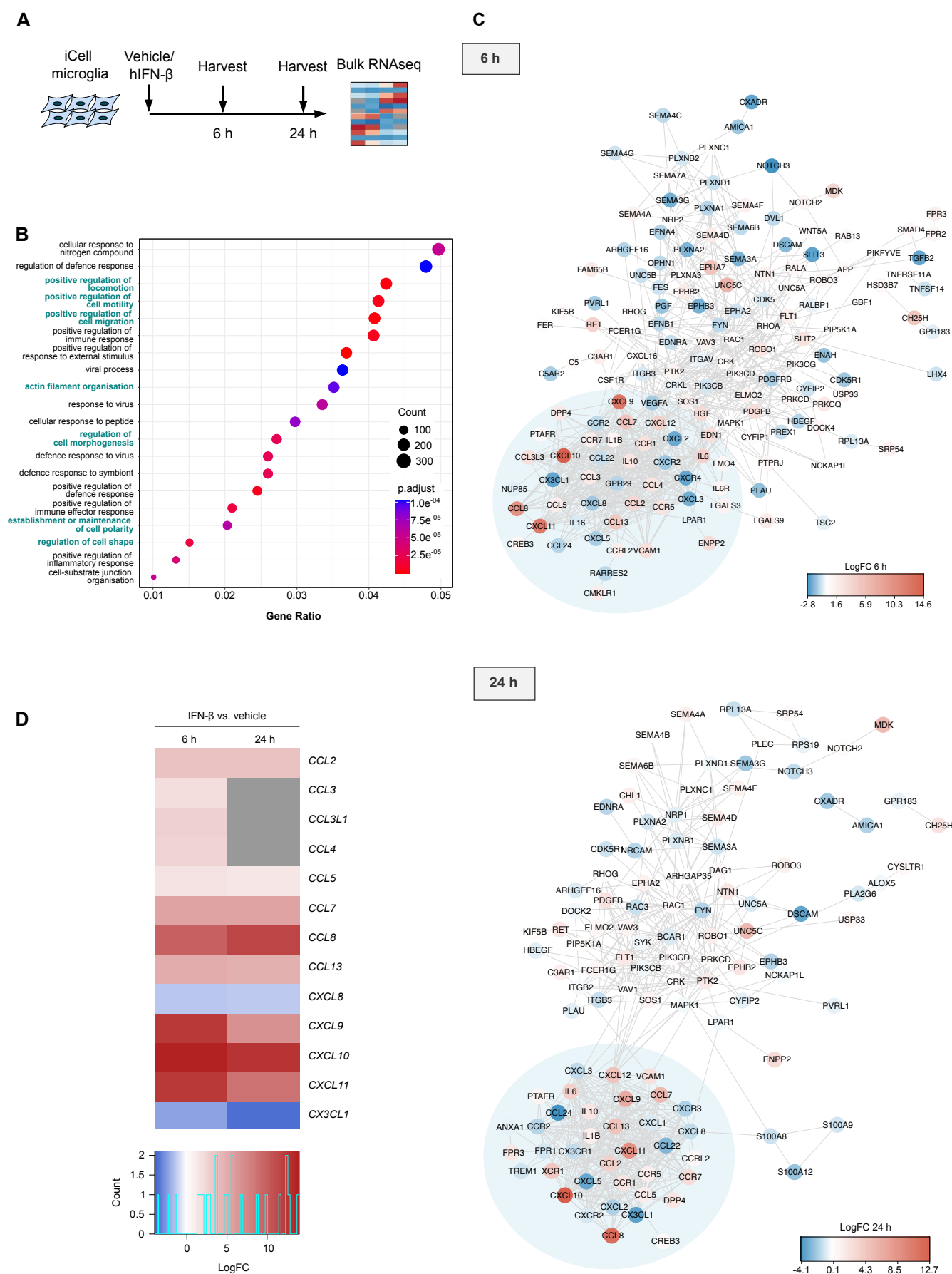
1047   **genome instability.**

1048   Persistent DNA damage, such as that observed in ATM deficiency, leads to formation of

1049   micronuclei in proliferating microglia. Activation of the cGAS-STING pathway culminates in

1050   IRF3 activation and production of type I interferons and chemokines, including *CCL5* and

1051   *CXCL10*. Secreted inflammatory mediators likely mediate a transition from homeostatic

1052   functions of microglia to chronic inflammation and chemotaxis to reactive microglia via

1053   autocrine and/or paracrine signalling, promoting chronic inflammation and chemotaxis.

1054   Blockade of STING rescues this process and has potential to alleviate perturbations to CNS
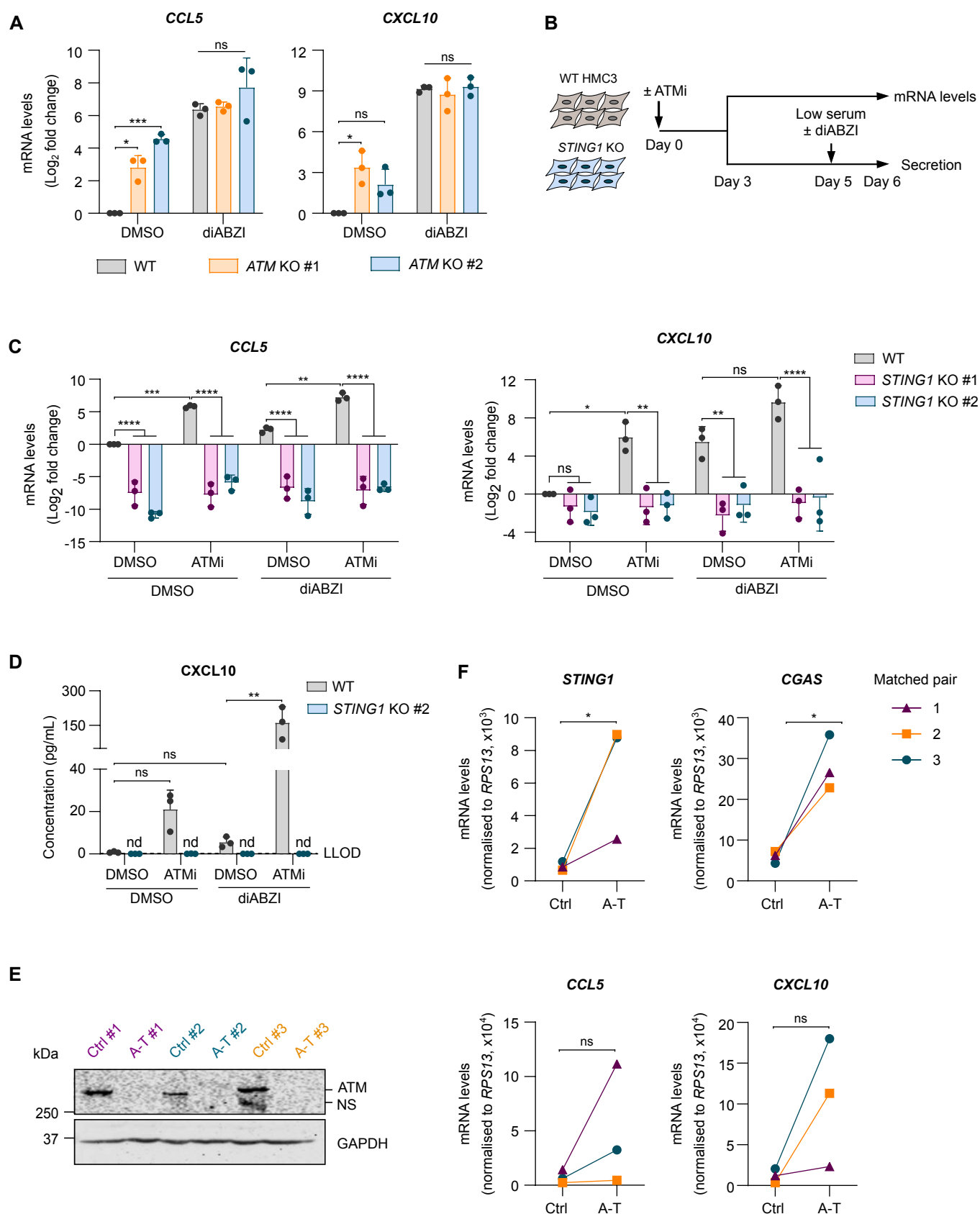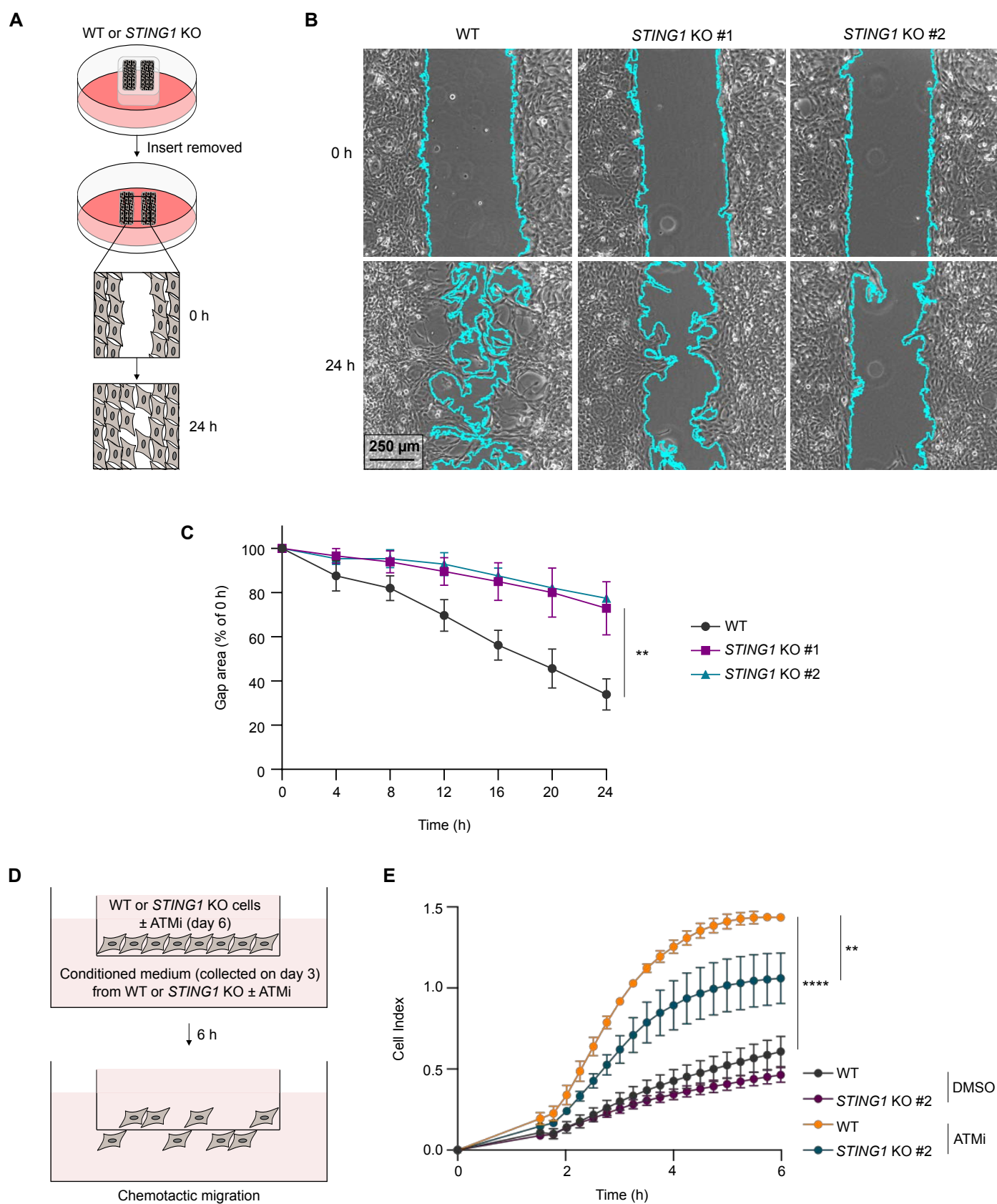
1055   homeostasis in genome instability.

Talbot *et al.*, Figure 1

Talbot *et al.*, Figure 2

Talbot *et al.*, Figure 3

Talbot *et al.*, Figure 4

Talbot *et al.*, Figure 5

Talbot *et al*., Figure 6

Talbot *et al.*, Figure 7